The Journal of Chemical Physics

An improved set of electron-THFA cross sections refined through a neural network-based analysis of swarm data

Cite as: J. Chem. Phys. **154**, 084306 (2021); https://doi.org/10.1063/5.0043759
Submitted: 11 January 2021 • Accepted: 28 January 2021 • Published Online: 24 February 2021

P. W. Stokes, S. P. Foster, M. J. E. Casey, et al.

COLLECTIONS

This paper was selected as an Editor's Pick

View Online Export Citation CrossMark

ARTICLES YOU MAY BE INTERESTED IN

Efficient enumeration of bosonic configurations with applications to the calculation of non-radiative rates
The Journal of Chemical Physics **154**, 084102 (2021); https://doi.org/10.1063/5.0039532

Spin relaxation in radical pairs from the stochastic Schrödinger equation
The Journal of Chemical Physics **154**, 084121 (2021); https://doi.org/10.1063/5.0040519

Explicit environmental and vibronic effects in simulations of linear and nonlinear optical spectroscopy
The Journal of Chemical Physics **154**, 084116 (2021); https://doi.org/10.1063/5.0038196

© 2021 Author(s).

AIP Publishing

The Journal of Chemical Physics ARTICLE scitation.org/journal/jcp

An improved set of electron-THFA cross sections refined through a neural network-based analysis of swarm data

Cite as: J. Chem. Phys. 154, 084306 (2021); doi: 10.1063/5.0043759
Submitted: 11 January 2021 • Accepted: 28 January 2021 •
Published Online: 24 February 2021

View Online Export Citation CrossMark

P. W. Stokes,[1,a] S. P. Foster,[1] M. J. E. Casey,[1] D. G. Cocks,[2] O. González-Magaña,[3] J. de Urquijo,[3] G. García,[4] M. J. Brunger,[5,6] and R. D. White[1]

AFFILIATIONS

[1]College of Science and Engineering, James Cook University, Townsville, QLD 4811, Australia
[2]Research School of Physics, Australian National University, Canberra, ACT 0200, Australia
[3]Instituto de Ciencias Físicas, Universidad Nacional Autónoma de México, 62251 Cuernavaca, Morelos, Mexico
[4]Instituto de Física Fundamental, CSIC, Serrano 113-bis, 28006 Madrid, Spain
[5]College of Science and Engineering, Flinders University, Bedford Park, Adelaide SA 5042, Australia
[6]Department of Actuarial Science and Applied Statistics, Faculty of Business and Management, UCSI University, Kuala Lumpur 56000, Malaysia

[a]**Author to whom correspondence should be addressed:** peter.stokes@my.jcu.edu.au

ABSTRACT

We review experimental and theoretical cross sections for electron transport in α-tetrahydrofurfuryl alcohol (THFA) and, in doing so, propose a plausible complete set. To assess the accuracy and self-consistency of our proposed set, we use the pulsed-Townsend technique to measure drift velocities, longitudinal diffusion coefficients, and effective Townsend first ionization coefficients for electron swarms in admixtures of THFA in argon, across a range of density-reduced electric fields from 1 to 450 Td. These measurements are then compared to simulated values derived from our proposed set using a multi-term solution of Boltzmann's equation. We observe discrepancies between the simulation and experiment, which we attempt to address by employing a neural network model that is trained to solve the inverse swarm problem of unfolding the cross sections underpinning our experimental swarm measurements. What results from our neural network-based analysis is a refined set of electron-THFA cross sections, which we confirm is of higher consistency with our swarm measurements than that which we initially proposed. We also use our database to calculate electron transport coefficients in pure THFA across a range of reduced electric fields from 0.001 to 10 000 Td.

Published under license by AIP Publishing. https://doi.org/10.1063/5.0043759

I. INTRODUCTION

The study of non-equilibrium electron transport in biological matter underpins a diverse range of scientific fields and applications. Of particular interest is the medical sector, where electron-induced processes in human tissue occur in both medical imaging and therapy.[1] In these applications, ionizing radiation liberates large numbers of low-energy secondary electrons (~30 eV), which undergo a variety of energy deposition processes in the biomolecules that constitute human tissue.[2] These thermalized electrons are known to undergo dissociative electron attachment (DEA), which has been attributed in part to the damage associated with such ionizing radiation, either directly through inducing single or double strand breaks in DNA or indirectly through the interactions of electron-induced radicals with DNA. Accurate kinetic simulations of electron transport in biological matter, including a full description of the interactions with each of the various biomolecular constituents, are therefore required in order to fully understand radiation damage and comprehensively inform dosimetry models.

Published under license by AIP Publishing

The modeling of electron transport in biomolecules has also found recent application in plasma medicine, which is a relatively new field motivated by the synergistic interactions of low-temperature atmospheric pressure plasmas (LTAPPs) with biological tissue.[3–5] Human tissue is generally modeled as a bulk liquid so that the system simplifies to a three-phase problem consisting of a bulk gas, a gas–liquid interface, and a bulk liquid.[4,5] While the interactions of the reactive oxygen and nitrogen species (RONS), produced in the plasma–liquid interface, are known to induce many of the synergistic effects,[3] a predictive understanding of plasma treatments can only be obtained through a complete understanding of all of the plasma–tissue interactions, including the electron-impact generation of radicals.[2]

Despite its importance, a full soft-condensed phase tissue description of electron transport is currently in its infancy. When applying kinetic modeling techniques, biological matter is currently approximated as water vapor, despite biological media being neither water nor a gas, nor being decoupled entirely from electron interactions as in plasma medical device modeling, but rather a complex mixture of biological molecules in a soft-condensed phase.[6–8] As such, quantitative modeling of electron transport through biological media requires the attainment of complete and accurate sets of cross sections for all electron interactions with all relevant biomolecules, including water, in the soft-condensed phase.

As low-energy electron interactions with DNA are difficult to study, focus has turned to the individual components of DNA, in addition to their structural analogs. One component that has received considerable attention is 2-deoxyribose, a sugar that links phosphate groups in the DNA backbone, which has well-studied surrogates including tetrahydrofuran (THF, C_4H_8O) and α-tetrahydrofurfuryl alcohol (THFA, $C_5H_{10}O_2$).[9] Between these, THF has received the most attention, with a number of proposed complete electron impact cross section sets present in the literature.[10–17] In comparison, however, while individual electron-THFA cross sections are known, a complete set is presently still lacking. In this investigation, we attempt to remedy this gap in the literature by constructing and refining a complete and self-consistent set of electron-THFA cross sections in the gas-phase, with the motivation being that such a set can be adapted to the soft-condensed phase through appropriate modifications using pair correlation functions.[18,19] The present investigation is especially warranted given that, in comparison to THF, THFA has been identified as a superior analog for 2-deoxyribose.[20,21]

Key to the derivation of our cross section set is the measurement and subsequent analysis of electron swarm transport coefficients in admixtures of THFA and argon. By comparing these measurements to simulated transport coefficients, the accuracy and self-consistency of our cross section set can be assessed.[22] Any discrepancies that are observed can then be used to inform appropriate adjustments to the cross sections in order to reduce the discrepancies with experiment. By iterating this process, such discrepancies can be minimized. This *inverse swarm problem* of unfolding cross sections from swarm measurements has a long and successful history.[23–30] However, being an inverse problem, it is often the case that there is no single unique set of cross sections that is consistent with a given set of swarm measurements. This nonuniqueness poses a fundamental challenge in automating swarm analysis using numerical optimization algorithms,[31–38] as while such algorithms diligently minimize the error in the associated transport coefficients, they lack the intuition about what constitutes a physically plausible cross section set. As such, to try and ensure the most success, these iterative adjustments to the cross section set must be carefully performed by an expert that can use their prior knowledge to rule out unphysical solutions. Despite these challenges, we have recently had some success in employing machine learning models to solve the inverse swarm problem automatically,[17,39] an approach that was originally explored by Morgan[40] decades earlier. By training these models on cross sections derived from the LXCat project,[41–43] they can, in a sense, "learn" what constitutes a physically plausible cross section set. Recently,[17] we trained an artificial neural network model in order to refine the electron-THF cross section set of de Urquijo *et al.*[16] Promisingly, the set of cross sections determined by this neural network was found to be of comparable quality to the set of de Urquijo *et al.* that was refined "by hand." LXCat cross sections have also been applied recently by Nam *et al.*[44] to train a neural network for the classification of cross sections according to their type (i.e., elastic, excitation, ionization, or attachment).

The remainder of this paper is structured as follows: In Sec. II, we briefly describe our data-driven approach to solving the inverse swarm problem, including the nature of the cross sections and transport coefficients used to train the machine learning model. Section III provides a review of existing electron-THFA cross sections in the literature. These measured and calculated integral cross sections (ICSs) are then employed to construct a "proposed" database for electron-THFA scattering, which is also described in this section. Note that several of the present authors have had recent experience in constructing databases for electron and positron scattering problems[45–48] but that the success of this approach does depend on the volume of relevant data available and by its very construction can be highly selective. In Sec. IV, details of our experimental technique for measuring the THFA-argon gas mixture transport coefficients are provided, with the results of these measurements also being presented. Note also in this section that results from our Boltzmann equation analysis, using our "proposed" cross sections, are provided and compared against the measured data. In Sec. V, a refined set of THFA electron scattering cross sections, using our machine learning/neural network-based approach, are presented and discussed, with results from their application in our Boltzmann equation analysis, for simulated transport parameters, being given in Sec. VI. Finally, Sec. VII presents our conclusions from the current investigation and gives some suggestions for future work.

II. NEURAL NETWORK FOR CROSS SECTION REGRESSION

In this section, we briefly describe the architecture and application of our neural network for the regression of electron-THFA cross sections from swarm transport data. For a more detailed description of this approach to inverting the swarm problem, we refer the reader to our previous publications (Refs. 39 and 17).

A. Neural network architecture

In this work, we perform the cross section regression by utilizing neural networks of the form

Published under license by AIP Publishing

$$\mathbf{y}(\mathbf{x}) = (\mathbf{A}_4 \circ \text{mish} \circ \mathbf{A}_3 \circ \text{mish} \circ \mathbf{A}_2 \circ \text{mish} \circ \mathbf{A}_1)(\mathbf{x}), \quad (1)$$

where $\mathbf{A}_n(\mathbf{x}) \equiv \mathbf{W}_n\mathbf{x} + \mathbf{b}_n$ are affine mappings, $\circ$ denotes the function composition, and $\text{mish}(x) = x\tanh(\ln(1+e^x))$[49] is a nonlinear *activation function* that is applied element-wise. The neural network [Eq. (1)] is said to be *fully connected* as the matrices of *weights*, $\mathbf{W}_n$, and vectors of *biases*, $\mathbf{b}_n$, are dense. The number of weights and biases is correlated with the *capacity* of the neural network to perform a particular nonlinear mapping from the input vector $\mathbf{x}$ to the output vector $\mathbf{y}$. With the exception of $\mathbf{b}_4$, the size of which must match the output of the network, we specify 256 biases per bias vector and size the weight matrices accordingly. Naturally, the output of our neural network for swarm analysis contains the electron-THFA cross sections of interest,

$$\mathbf{y} = \begin{bmatrix} \sigma_1(\varepsilon) \\ \sigma_2(\varepsilon) \\ \vdots \end{bmatrix}. \quad (2)$$

As these cross sections are functions of energy, we accordingly include the energy ε as an element of the input vector $\mathbf{x}$. To solve the inverse swarm problem, we populate the remaining input elements with the swarm transport coefficient measurements,

$$\mathbf{x} = \begin{bmatrix} \varepsilon \\ W_1 \\ W_2 \\ \vdots \\ (\alpha_{\text{eff}}/n_0)_1 \\ (\alpha_{\text{eff}}/n_0)_2 \\ \vdots \\ (n_0 D_L)_1 \\ (n_0 D_L)_2 \\ \vdots \end{bmatrix}, \quad (3)$$

where W denotes the drift velocity, α_{eff} denotes the effective Townsend first ionization coefficient, D_L denotes the longitudinal diffusion coefficient, and n_0 is the background neutral number density.

Cross section regression in this way is particularly appealing due to the versatility of neural networks. So long as the energy ε remains an input to the network, we can in principle derive cross sections from any collection of experimental measurements. In fact, in forming our initial proposed set of electron-THFA cross sections in Sec. III, we derive plausible vibrational and electronic excitation cross sections in this way from the limited number of experimental measurements that are currently available.

It should finally be noted that we normalize all inputs and outputs of the neural network by first taking the logarithm and then performing a linear mapping onto the domain $[-1,1]$. As a consequence of this log-transformation, we are restricted to inputs and outputs that are positive. This poses a difficulty when predicting cross sections below the threshold. In such instances, we replace cross sections equal to zero with a suitably small positive number, which we take to be 10^{-26} m^2. Consequently, if the neural network outputs a cross section less than 10^{-26} m^2, we interpret the output as zero. This allows the threshold energy to be determined implicitly from the output of the neural network.

B. Training data

For training the neural network [Eq. (1)], we use, as required, elastic, excitation, ionization, and attachment cross sections from the LXCat project.[41–43,50–68] Specifically, we generate realistic cross sections for training by taking random pairwise geometric combinations of cross sections from LXCat using the formula

$$\sigma(\varepsilon) = \sigma_1^{1-r}\left(\varepsilon + \varepsilon_1 - \varepsilon_1^{1-r}\varepsilon_2^{r}\right)\sigma_2^{r}\left(\varepsilon + \varepsilon_2 - \varepsilon_1^{1-r}\varepsilon_2^{r}\right), \quad (4)$$

where $\sigma_1(\varepsilon)$ and $\sigma_2(\varepsilon)$ are cross sections of a given process chosen randomly without replacement, ε_1 and ε_2 are their respective threshold energies, and $r \in [0,1]$ is a uniformly sampled mixing ratio. We apply similar geometric combinations when we wish to constrain training cross sections within known experimental error bars. Specifically, we ensure that $\sigma_1(\varepsilon)$ is itself constrained and then perturb about it with a random $\sigma_2(\varepsilon)$ and a mixing ratio r chosen small enough so as not to violate the prescribed constraints.

Once cross sections have been selected for training, they must be sampled at various energies within the domain of interest. In this work, we are concerned with the domain $\varepsilon \in \left[10^{-3}\text{ eV}, 10^{3}\text{ eV}\right]$, which we sample randomly within using

$$\varepsilon = 10^{s}\text{ eV}, \quad (5)$$

where $s \in [-3,3]$ is a uniformly distributed random number.

To complete the input vector of our input/output training pair, we calculate corresponding transport coefficients using a well-benchmarked multi-term solution of Boltzmann's equation.[22,69,70] For good measure, we employ the ten-term approximation for all cross section sets used for training. Additionally, to simulate the random error present in the experimental swarm measurements, we multiply our simulated transport coefficients by a small amount of random noise sampled from a log-normal distribution. Specifically, we sample the natural logarithm of this noise factor from a normal distribution with a mean of 0 and a standard deviation of 0.03.

C. Training procedure

The neural network is implemented and trained using the *Flux.jl* machine learning framework.[71] Before training, we initialize the neural network biases to zero and weights to uniform random numbers as described by Glorot and Bengio.[72] Then, to train the network, we perform numerical optimization of its weights and biases so as to minimize the mean absolute error of the cross sections fitted by the neural network. We choose the mean absolute error measure due to its robustness in the presence of outliers. During the optimization, we repeatedly update the weights and biases using the Adam optimizer[73] with step size $\alpha = 10^{-3}$, exponential decay rates $\beta_1 = 0.9$ and $\beta_2 = 0.999$, and small parameter $\epsilon = 10^{-8}$. For each update of the neural network parameters with the optimizer, we consider a random batch of 4096 input/output training examples.

Published under license by AIP Publishing

Each of these batches consist of 16 random LXCat-derived cross section sets, with each set sampled at 256 random energies using Eq. (5). In total, the training dataset consists of 50 000 unique sets of cross sections. Training is continued until the transport coefficients resulting from the fitted cross section set best match the measured pulsed-Townsend transport coefficients that were used to perform the fit.

III. ELECTRON-THFA CROSS SECTION DATA REVIEW AND INITIAL PROPOSALS

A. Electronic excitation cross sections

Electronic-state scattering results for electron-THFA includes the experimental differential cross section (DCS) data of Chiari *et al.*[74] and the corresponding integral cross section (ICS) data of Duque *et al.*,[21] the latter of which are plotted in Fig. 1. These authors identify five Rydberg electronic-state bands for THFA,[20] although due to insufficient energy resolution in the experimental apparatus, these are resolved into only three separate electronic-state bands. These bands are reported as having threshold energies of 6.2, 7.6, and 8.2 eV for bands 1 + 2, band 3, and bands 4 + 5, respectively. To construct our proposed electronic excitation cross sections for THFA, we make use of these threshold energies alongside the ICS data of Duque *et al.* To interpolate these data, as well as extrapolate to higher energies, we employ a neural network of the form of Eq. (1) to fit a plausible excitation cross section for each case. Specifically, for a given band, we input to the network the ICS data at the four energies considered by Chiari *et al.* and Duque *et al.* (20, 30, 40, and 50 eV), as well as the threshold energy for that band. The resulting neural network regression, and initial proposed ICS, for each band is plotted in Fig. 1. In each case, a plausible energy location of the peak cross section value is identified automatically by the network.

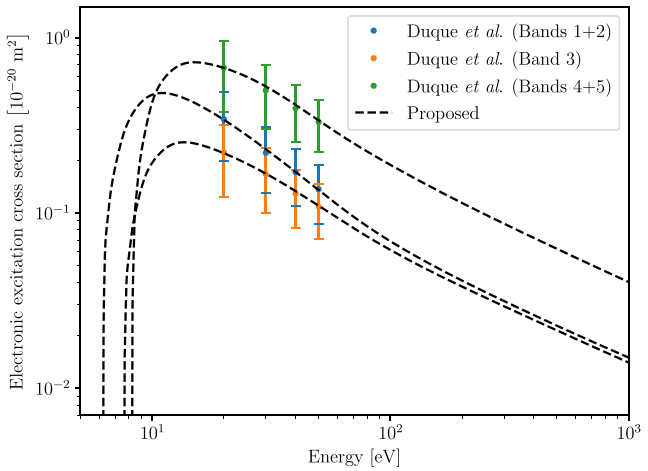

FIG. 1. Proposed THFA discrete electronic excitation cross sections, alongside the experimental measurements[21] to which our initial proposals were fitted. See also the legend in the figure.

B. Vibrational excitation cross sections

Vibrational scattering data for electron-THFA consists only of the experimental DCS and ICS data of Duque *et al.*,[75] at the incident energies of 20, 30, 40, and 50 eV. The four vibrational modes of THFA identified by Duque *et al.* are the CC stretch, CH_2 stretch, OH stretch + combination band, and 2 × CH_2 stretch overtone, with respective threshold energies of approximately 0.12, 0.33, 0.5, and 0.7 eV. For our proposed THFA vibrational excitation cross sections, we make use of these ICS data with these corresponding energy thresholds. At lower energies, we employ the THF data of Khakoo *et al.*[76] for the same vibrational modes, defined at the energies 2, 10, 15, and 20 eV. Note that, here, we scale the data of Khakoo *et al.* a little, so as to match the THFA data of Duque *et al.* at the overlapping point of 20 eV. This approach is thought to be reasonable due to THF and THFA having similar structures and intrinsic molecular properties (e.g., dipole moment and dipole polarizability). At very low energies, down to the threshold in each case, we make use of the THF CC stretch data of Allan.[77] To accomplish this, we need to shift Allan's measurement to each respective THFA threshold and also to scale so as to minimize the discontinuity with the overlapping scaled measurements of Khakoo *et al.* We then subsequently performed a smoothing cubic spline interpolation[78] through the measurements of Duque *et al.*, the scaled measurements of Khakoo *et al.*, and the shifted and scaled measurement of Allan *et al.* (up to 1 eV above threshold in each case). Finally, above 50 eV, we employ the same neural network regression approach used in Sec. III A for electronic excitation interpolation/extrapolation. Specifically, for each vibrational mode, we consider as input to that neural network the threshold energy and the four measurements of Duque *et al.* in each case. The output of the neural network is then the vibrational integral cross section at points above 50 eV (up to 1000 eV). We join the resulting high-energy extrapolation with the smoothing cubic spline interpolation at 50 eV by a further scaling. The final proposed vibrational excitation cross sections for THFA are plotted in Fig. 2, alongside all of the experimental measurements from which they are derived.

C. Electron impact ionization cross section

Available scattering data for electron impact ionization of THFA include the theoretical ICS data of Możejko and Sanche,[79] the experimental ICS results of Bull *et al.*,[80] and the theoretical ICS data of Duque *et al.*[21] These are each plotted in Fig. 3. Both of the aforementioned theoretical investigations use a semi-classical binary-encounter-Bethe (BEB) formalism,[21,79,81] with Duque *et al.* also having employed a modified IAM-SCAR approach.[21] The modification used by Duque *et al.* was originally proposed in Ref. 82 and allows the separation of the ionization ICS from the total "inelastic" ICS provided by the IAM-SCAR approach. The data of Bull *et al.* are determined from measurements of ion and electron currents using the Beer–Lambert law[80] and agree quite well with the BEB results in terms of both their shape and the position of the cross section maximum, while being generally lower in magnitude compared to the theoretical results. As the sole experimental data available, and from a group with a long history of making reliable ionization cross section measurements, we use the ionization ICS of Bull *et al.*

Published under license by AIP Publishing

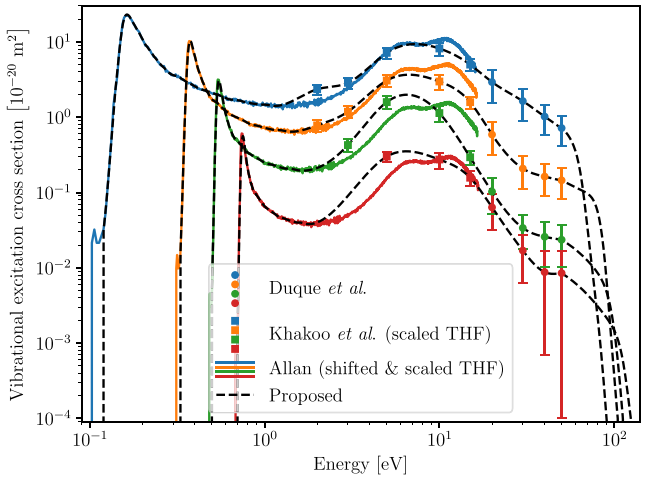

FIG. 2. Proposed vibrational excitation cross sections, alongside the experimental measurements[75–77] to which our initial proposed data were fitted. The four vibrational modes here are CC stretch (blue), CH_2 stretch (orange), OH stretch + combination (green), and 2 × CH_2 stretch (red). See also the legend in the figure.

as the basis for our proposed ionization cross section. For energies above the maximum considered by Bull *et al.* (285 eV), we make use of the modified IAM-SCAR results of Duque *et al.* For energies below the minimum considered by Bull *et al.* (10 eV), we specify an ionization threshold of 9.69 eV, as was obtained by Dampc *et al.*[83] through the analysis of THFA photoelectron spectra. This resulting initial proposed ionization cross section can also be found plotted in Fig. 3.

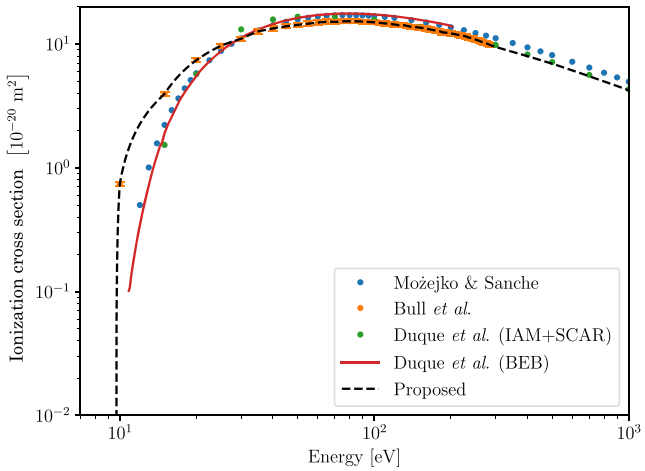

FIG. 3. Proposed electron impact ionization cross section, alongside previous experimental and theoretical results[21,79,80] from which it was derived. See also the legend in the figure.

D. Electron attachment cross section

To our knowledge, there are currently no attachment scattering data available for THFA in the literature. There are, however, dissociative electron attachment (DEA) cross sections available for some other structurally similar biomolecules, including THF[10,15–17,84,85] and 3-hydroxytetrahydrofuran (3-hTHF),[84] from which we can obtain a very rough initial estimate for that of THFA. Brunger[9] noted that the most important electronic-structure quantities for determining the relative magnitude of DEA cross sections between biomolecules are the dipole moment and dipole polarizability of each molecule, with the dipole polarizability being the most significant. While of course this is very much a first order approximation, it does provide at least some physical basis to what follows. On average, across all five of its conformers at room temperature,[20] THFA has a large dipole polarizability of ~ $63.38a_0^3$,[20,21] where a_0 is the Bohr radius. For construction of our proposed electron attachment cross section for THFA, we prioritize using the available 3-hTHF DEA data over that for THF, as both 3-hTHF and THFA contain a hydroxyl group, the presence of which has been shown experimentally to enhance DEA.[84] Specifically, we choose to use the 3-hTHF DEA measurement of Aflatooni *et al.*[84] Compared to THFA, 3-hTHF has an average dipole polarizability of ~ $50.8281a_0^3$,[86,87] a value we obtain simply by averaging the theoretically determined values of its two most energetically stable conformers of $50.6779a_0^3$ and $50.9782a_0^3$.[86] Accordingly, we scale up the 3-hTHF DEA measurement of Aflatooni *et al.* by the ratio between the THFA and 3-hTHF dipole polarizabilities (×1.247). This then completes the DEA component of our proposed attachment cross section. At energies below 0.1 eV, where DEA is impossible and any attachment is inherently non-dissociative, we make use of the electron attachment cross section for THF derived by Stokes *et al.*[17] using a neural network-based analysis of swarm transport data. Of course, it is also necessary to scale this cross section (×52.71) so that the peak magnitude for DEA matches that for the scaled 3-hTHF DEA measurement used at higher energies. Finally, we perform a smoothing cubic spline interpolation[78] over the entire range being considered. The resulting proposed electron attachment cross section for THFA can be found plotted in Fig. 4, alongside the scaled THF and 3-hTHF counterparts it was derived from.

E. Grand total cross section

Grand total cross section (TCS) scattering data for electron-THFA include the theoretical TCS results from Milosavljević *et al.*,[88] the experimental TCS data of Możejko *et al.*,[89] the theoretical TCS data of Zecca *et al.*,[90] and the theoretical TCS data of Duque *et al.*[21] These are summarized in Fig. 5. The experimental data of Możejko *et al.* are derived by applying the Beer–Lambert formula,[89] to the attenuated and unattenuated electron beam intensities, in a linear transmission experiment. Those data are not corrected for the forward-scattering effect[89] and are therefore expected to be missing the significant effect of the rotational cross sections at lower energies. The theoretical data of Milosavljević *et al.* are calculated using the IAM-SCAR approach, which yields combined elastic, electronic excitation, neutral dissociation, and ionization processes, while lacking contributions from rotational, vibrational excitation, and DEA processes. The TCS data of Zecca *et al.* are calculated using the

Published under license by AIP Publishing

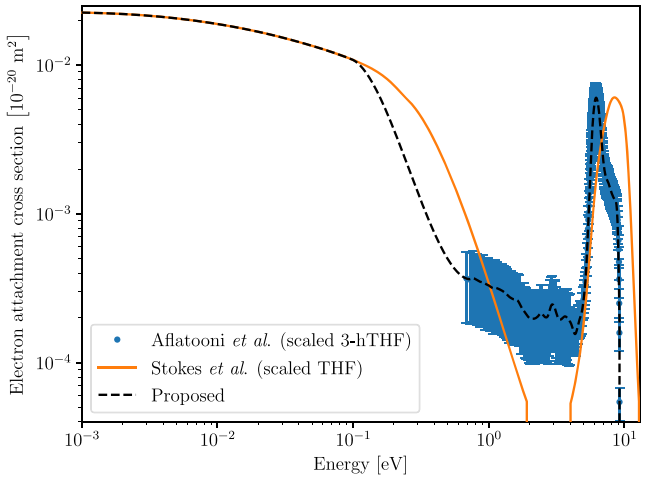

FIG. 4. Proposed electron attachment cross section, alongside the previous results[17,84] from which it was derived. See also the legend in the figure.

IAM-SCAR + R procedure and include all processes except for vibrational excitation and DEA. Here, rotational excitation is included using a Born approximation-based method. The data of Duque *et al.* are also calculated using the IAM-SCAR + R procedure, but the innovation of Chiari *et al.*[82] is also employed in this case to separate the ionization channel from the rest of the "inelastic" data. The TCS data of Duque *et al.* therefore also include all processes except for vibrational excitation and DEA but are able to individually resolve the elastic, rotational, discrete electronic-state excitation, and ionization cross sections. For our proposed grand TCS for THFA, we prioritize the experimental data of Możejko *et al.* over the theoretical results. However, to use these data, we must first correct for the forward-scattering effect by increasing the magnitude of this cross section at lower energies. To determine the extent of this correction, we use the TCS data of Duque *et al.* as a guide, to which we add our proposed vibrational excitation and DEA cross sections to form an initial approximate grand TCS. Next, we scale the experimental data of Możejko *et al.* so as to best match this approximation. In particular, we scale by an energy-dependent correction of the power-law form $1 + 5.169\varepsilon^{-1.050}$, which has the greatest effect at smaller energies, while leaving the experimental data at higher energies unaffected. At energies above 370 eV, we use the same approximate grand TCS data derived from Duque *et al.* but scaled down (×0.88) so as to improve continuity with the experimental data of Możejko *et al.* The resulting proposed grand TCS is plotted in Fig. 5, alongside the various results from the literature.[21,88–90]

F. Rotational cross section

Rotational scattering data for electron-THFA collisions include the theoretical ICS data of Zecca *et al.*[90] and the theoretical ICS data of Duque *et al.*[21] These are plotted in Fig. 6. Both of these rotational cross sections are derived using the first Born approximation (FBA), with Zecca *et al.* having calculated the rotational excitation cross section, for $J \to J'$ in THFA at 300 K, by weighting the population for the Jth rotational quantum number at that temperature and estimating the average excitation energy from the corresponding rotational constants. On the other hand, Duque *et al.* used the procedure of Jain.[91] All the integral rotational cross section data are given in terms of a single summed rotational cross section, with the ICS data of Duque *et al.* calculated from assuming an average rotational threshold energy of 0.74 meV. As we are relying on the TCS data of Duque *et al.* to guide the form of our proposed grand TCS, for consistency, we also make use here of the data from Duque *et al.* for our proposed rotational ICS, as shown in Fig. 6.

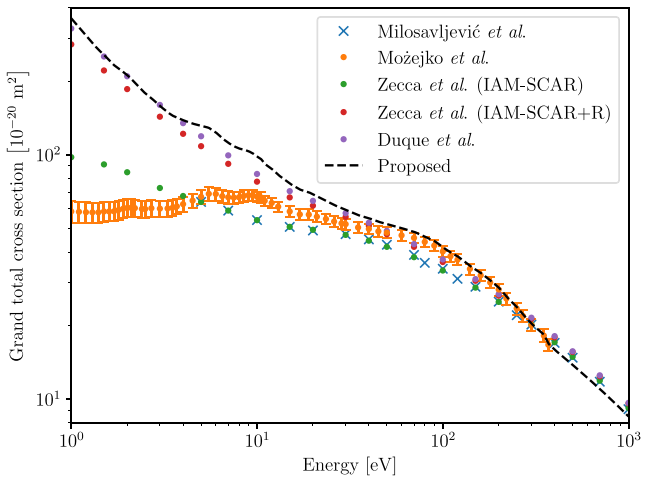

FIG. 5. Proposed grand total cross section, alongside previous experimental and theoretical total cross sections.[21,88–90] See also the legend in the figure.

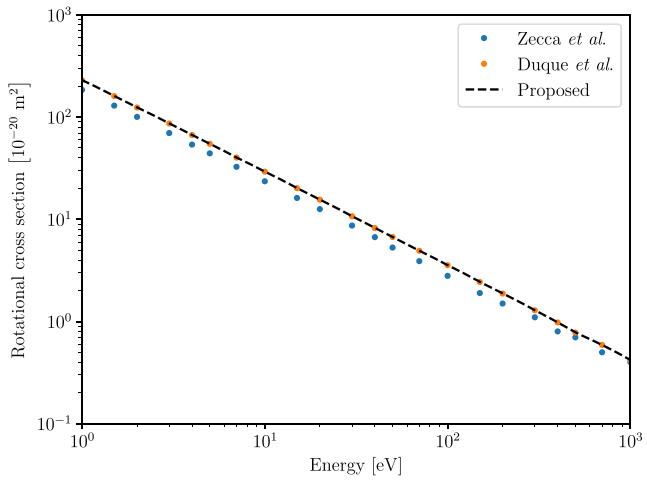

FIG. 6. Proposed rotational integral cross section, alongside previous theoretical results.[21,90] See also the legend in the figure.

Published under license by AIP Publishing

G. Elastic cross section

Elastic scattering data for electron-THFA collisions include the theoretical DCS and ICS data of Możejko and Sanche,[79] the theoretical ICS data of Milosavljević *et al.*,[88] and the theoretical ICS data of Duque *et al.*[21] These are summarized in Fig. 7. The calculations of Możejko and Sanche are performed using the independent-atom method (IAM), are applied with the additivity rule (AR), and have been superseded by the calculations of Milosavljević *et al.* and Duque *et al.*, which use the IAM-SCAR procedure, that is, the IAM in conjunction with a screening corrected additivity rule (SCAR). The ICS data of both Milosavljević *et al.* and Duque *et al.* are in good agreement with one another, and as such, we base our proposed THFA elastic ICS on both of these results, with some minor modifications in place for consistency with our proposed grand TCS. The resulting proposed elastic ICS is plotted in Fig. 7. Even by accounting for all of the cross sections proposed thus far (outlined in Secs. III A–III G), there still remains a discrepancy in the grand TCS at intermediate energies, which we attribute to neutral dissociation, as discussed in Sec. III H.

H. Neutral dissociation cross section

A challenge in obtaining complete sets of electron-biomolecule cross sections is the intractability of determining the neutral dissociation integral cross section from scattering experiments directly.[92] Similarly, theoretical results are rare.[48] Of course, in principle, it can be found indirectly by subtracting all the other scattering cross sections from the TCS, resulting in a remnant that is attributed to neutral dissociation. Proceeding with this approach results in the proposed THFA neutral dissociation cross section plotted in Fig. 8, with an apparent threshold energy of 18.4 eV. However, as the accuracy of this remnant is predicated on the collective accuracy of all other cross sections outlined thus far, it is not anticipated to be particularly reliable. As an alternative to this approach, swarm experiments provide an implicit way of elucidating the neutral dissociation cross section through assessment of the self-consistency of a cross section set. Indeed, the neutral dissociation cross section of THF has previously been characterized through the swarm analysis of Casey *et al.*[15] and de Urquijo *et al.*,[16] as well as recently by Stokes *et al.*[17] using the same machine learning formalism described in Sec. II and employed later in Sec. V of the present investigation.

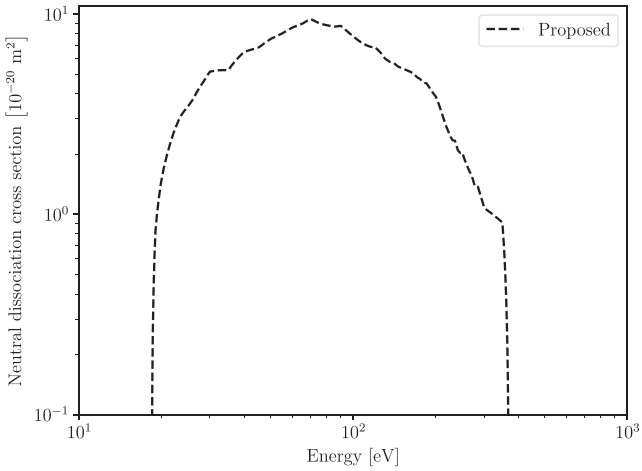

FIG. 8. Proposed neutral dissociation cross section. See text for further details.

I. Quasielastic momentum transfer cross section

For the purposes of performing transport calculations, we form a proposed quasielastic (elastic + rotational) momentum transfer cross section (MTCS) by scaling our proposed quasielastic ICS by

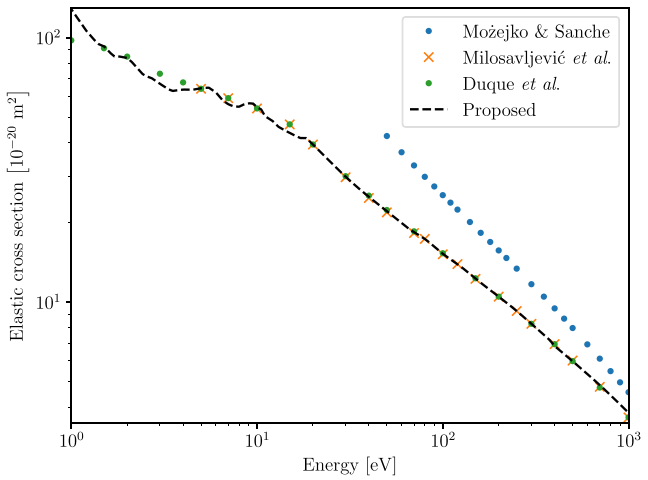

FIG. 7. Proposed elastic integral cross section, alongside previous theoretical results.[21,79,88] See also the legend in the figure.

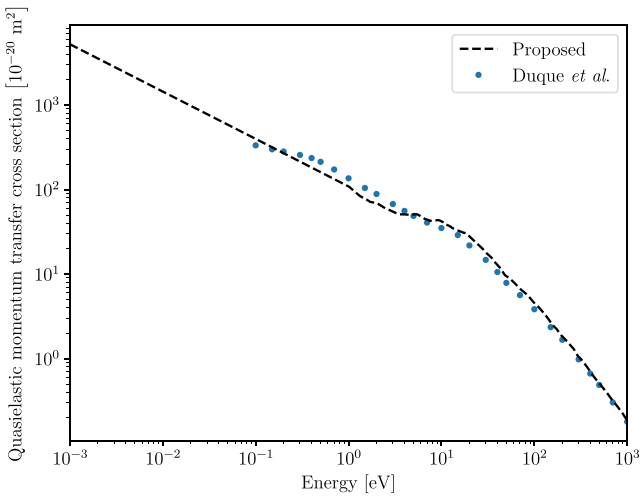

FIG. 9. Proposed quasielastic momentum transfer cross section. See text for further details.

Published under license by AIP Publishing

the ratio of quasielastic MTCS to ICS of Duque *et al.*[21] At energies below 1 eV, we utilize a power-law extrapolation that is fitted to the quasielastic MTCS of Duque *et al.* in this regime. Our resulting proposed quasielastic MTCS is plotted in Fig. 9.

IV. PULSED-TOWNSEND SWARM MEASUREMENTS FOR ASSESSING THE SELF-CONSISTENCY OF THE PROPOSED CROSS SECTION SET

To assess the quality of our proposed set of electron-THFA cross sections, we perform a number of pulsed-Townsend swarm experiments from which we obtain drift velocities, effective Townsend first ionization coefficients, and longitudinal diffusion coefficients for admixtures of THFA in argon. We consider mixture ratios of 0.2%, 0.5%, 1%, 2%, and 5% THFA, across a range of reduced electric fields, from 1 to 450 Td, where 1 Td = 1 Townsend = 10^{-21} V m^2. The results from these measurements—which are tabulated in our Appendix, Tables I–V—were derived from a pulsed-Townsend apparatus whose technique and methods of analysis of the electron avalanche waveforms have been accounted for in detail previously.[93,94] The pulsed-Townsend method is based on the measurement of the total displacement current due to the motion of electrons and ions within a parallel plate capacitor that produces a highly homogeneous field upon the application of a highly stable and very low ripple DC voltage between 150 V and 5 kV, depending on the E/n_0 and n_0 conditions of the experiment. The capacitor through which the charge carriers drift and react consists of an aluminum cathode and a non-magnetic stainless steel anode of 12 cm diameter each, separated by an accurately measured distance of 3.1 cm to within an accuracy of 0.025 mm. The initial photoelectrons are generated from the cathode by the incidence of a UV laser pulse (1 mJ–2 mJ, 355 nm, 3 ns). When the dominant processes involved in the avalanche are due to the electrons and stable, non-reacting, ions then any collisional ionization or attachment events are due only to electrons. Furthermore, since the electron drift velocity is 10^2–10^3 times larger than that of the ions, the resulting total current can readily be separated into a fast component due mostly to the electrons, followed by that of the slower ions. The analysis of the electron component leads to the derivation of the flux electron drift velocity, W, and the density-normalized effective ionization coefficient, $\alpha_{\text{eff}}/n_0 = (\alpha - \eta)/n_0$, where α and η are the ionization and electron attachment coefficients. A very stable voltage in the range 0.2–5 kV was applied to the anode in order to produce the highly homogeneous electric field E, according to the E/n_0 value selected and the gas density n_0 in the discharge vessel. The stated purity of the commercial THFA sample used was 99.0% (Sigma-Aldrich) and that of Ar was 99.995% (Praxair). Because of the very low vapor pressure of THFA, namely, 0.2 Torr at 293 K, the maximum pressure allowed in the discharge vessel was 0.18 Torr. This very low filling pressure value hindered the measurements of the electron swarm coefficients for pure THFA. The mere presence of the electron avalanche produces a space charge field, which is superposed to the externally applied one. Thus, care must be taken to keep the minimum external voltage high enough so that the space charge field is smaller than 1% of that applied to the anode. With the present configuration, with an interelectrode distance of 3.1 cm, we could only measure THFA mixtures with Ar successfully from 0.2% to 5% THFA. The minimum external voltage was 200 V. The measurements were performed at room temperature in the range 293 K–300 K, measured with a precision of ±0.5 K, while the gas mixture pressure was monitored with an absolute pressure capacitance gauge (±0.15% uncertainty). The displacement current due to the electrons was measured with a very low-noise, 40 MHz amplifier with a transimpedance of 10^5 V/A. The measured electron transients were analyzed using the formula for the electron current in the external circuit derived by Brambring,[95]

$$I(t) = \frac{n_0 q W}{2L} e^{\alpha_{\text{eff}} W t} \left\{ \text{erfc}\left[\frac{(W + \alpha_{\text{eff}} D_L)t - L}{\sqrt{4 D_L t}} \right] - e^{\frac{W + \alpha_{\text{eff}} D_L}{D_L} L} \text{erfc}\left[\frac{(W + \alpha_{\text{eff}} D_L)t + L}{\sqrt{4 D_L t}} \right] \right\}, \tag{6}$$

where L is the drift distance and $\text{erfc}(x) = 1 - \frac{2}{\sqrt{\pi}} \int_0^x e^{-u^2} du$ is the complementary error function. Thus, we have three swarm parameters to determine, namely, W, α_{eff}, and D_L. The process is simplified by determining initial values of W and α_{eff}, derived from a basic, geometrical analysis[96,97] and inserted into a simulator to fit the whole transient, thereby obtaining D_L and refined values of α_{eff} and W. Typical uncertainties for W, α_{eff}, and D_L were ±2%, ±6%, and ±12%, respectively. Note that these transport coefficients can be related to the net ionization frequency, R_{net}; the bulk drift velocity, W_B; and the bulk diffusion coefficient, $D_{B,L}$, via[98]

$$R_{\text{net}} = \alpha_{\text{eff}} W, \tag{7}$$

$$W_B = W + \alpha_{\text{eff}} D_L, \tag{8}$$

$$D_{B,L} = D_L. \tag{9}$$

Using our proposed cross section set, we apply a well-benchmarked multi-term solution of Boltzmann's equation[22,70,99] to derive simulated pulsed-Townsend transport coefficients for comparison to our admixture measurements. For calculating these admixture transport coefficients, we use the argon cross section set present in the Puech database[65] on LXCat.[41–43] The simulated transport coefficients are plotted alongside the experimental values in Fig. 10. Figure 10(a) compares the drift velocities and shows qualitative agreement at low-to-intermediate fields, with the proposed dataset underestimating its magnitude slightly at the highest fields considered. Interestingly, while both measured and simulated drift velocities exhibit negative differential conductivity (NDC)—drift velocity decreasing with increasing reduced electric field—there is disagreement in the extent of NDC, with the simulated drift velocities exhibiting NDC over a much larger range of fields. Figure 10(b) compares the effective Townsend first ionization coefficients and shows that those that result from the proposed set overestimate the magnitude in the electropositive regime and underestimate the magnitude in the electronegative regime. That is, overall, the simulated effective Townsend first ionization coefficients are too positive, suggesting that an increase in the magnitude of the proposed attachment cross section is required, as well as a decrease in the magnitude of

Published under license by AIP Publishing

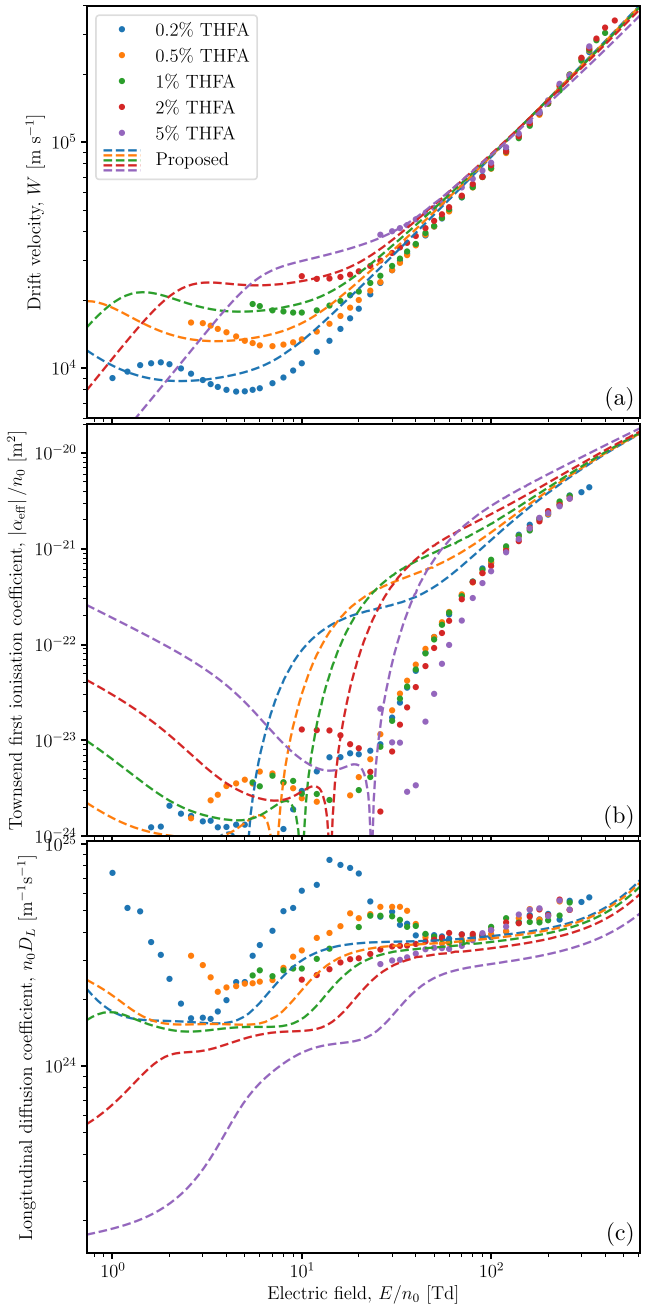

FIG. 10. Measured pulsed-Townsend swarm transport coefficients (markers) of (a) the drift velocity, W, (b) the effective Townsend first ionization coefficients, α_{eff}/n_0, and (c) the longitudinal diffusion coefficients, $n_0 D_L$. Simulated transport coefficients (dashed curves), derived from the proposed cross section set presented in Sec. III, are also plotted for comparison.

the proposed ionization cross section. Figure 10(c) compares the longitudinal diffusion coefficients and shows the poorest agreement between simulation and experiment across all of the considered transport coefficients with the simulated diffusion coefficients consistently underestimating the measurements. Fortunately, the general shape of the simulated diffusion coefficients appears to be in fair qualitative agreement with experiment.

V. REFINED ELECTRON-THFA CROSS SECTIONS

Given the results in Fig. 10, we now employ the neural network model [Eq. (1)] to solve the inverse problem of mapping from our admixture swarm measurements to a selection of desired electron-THFA cross sections. Specifically, we choose to fit the neutral dissociation cross section, electron attachment cross section, electron impact ionization cross section, and quasielastic MTCS. By replacing those cross sections in our earlier proposed set, with those predicted by the neural network, we complete our refined set of electron-THFA cross sections.

A. Refined neutral dissociation cross section

As very little can be stated about the nature of neutral dissociation in THFA, we choose to place no explicit constraints on the neutral dissociation cross section when training the neural network, thus forming training data, using Eq. (4), to directly combine random pairs of excitation cross sections from the LXCat project. The resulting confidence band of training examples is plotted in Fig. 11, alongside the subsequent refined fit provided by the neural network, as well as the original proposed cross section for comparison. Compared to that which was proposed originally, the neural network predicts a neutral dissociation cross section that is substantially smaller in magnitude, peaking at 8.4×10^{-24} m^2 vs 9.4×10^{-20} m^2, while also having a smaller threshold energy, with a value of 3.96 vs 18.4 eV. Promisingly, the neural network has also resolved a plausible high-energy tail—a feature that is lost when determining neural dissociation as a residual of the grand TCS.

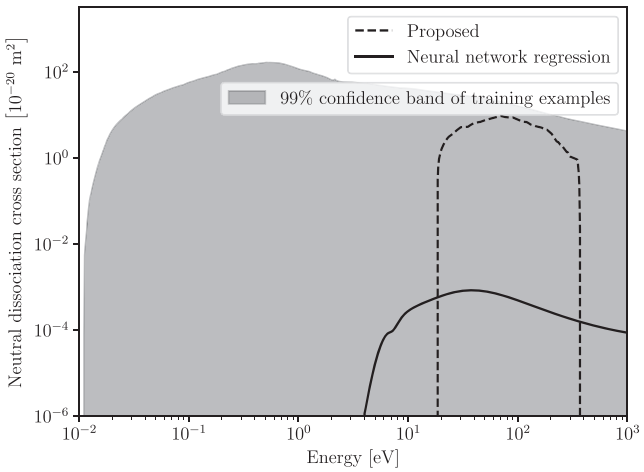

FIG. 11. Neural network regression results for the THFA neutral dissociation cross section, alongside the earlier proposed ICS for comparison. See also the legend in the figure.

Published under license by AIP Publishing

B. Refined electron attachment cross section

Due to the current lack of electron-THFA attachment data in the literature, the attachment cross sections used for training the neural network are chosen in a similarly unconstrained fashion as those used to refine neutral dissociation. That is, Eq. (4) is used to combine random pairs of LXCat attachment cross sections for training, while enforcing no additional explicit cross section constraints. The resulting confidence band of training examples is plotted in Fig. 12, alongside the refined fit provided by the neural network, as well as the original proposed attachment cross section. The neural network predicts an attachment cross section that is more uniform than that which was proposed initially, thus resulting in some substantial differences in different energy regimes. For example, at low energies, near 10^{-3} eV, the refinement is over two orders of magnitude smaller than the initial proposal. At intermediate energies, around 3 eV, the refinement rises slightly in magnitude while the proposal drops significantly, resulting in the refinement exceeding the proposal by almost an order of magnitude. Both the refinement and the initial proposal have a peak near 6 eV, although the refined attachment cross section has a peak magnitude that is almost a factor of 4 smaller than that for the initial proposal. At higher energies, past this peak, both attachment cross sections decay fairly rapidly in magnitude, with practically no attachment beyond 12 eV in the refinement, compared to 10 eV for the original proposed data.

C. Refined electron impact ionization cross section

Given the general agreement among the ionization cross sections reviewed thus far, we choose to constrain the ionization training examples to within the vicinity of our resulting initial proposal. We make these constraints particularly stringent at higher energies, where the theoretical results are expected to be more accurate and where our swarm analysis is expected to be less informative. Across all training examples, we use the same threshold energy of 9.69 eV, as was done for our initial proposed ionization cross section. Consequently, the ionization training cross sections are formed using a formula very similar to Eq. (4),

$$\sigma(\varepsilon) = \sigma_1^{1-r(\varepsilon)}(\varepsilon)\sigma_2^{r(\varepsilon)}(\varepsilon + \varepsilon_2 - 9.69\ \text{eV}), \tag{10}$$

where $\sigma(\varepsilon)$ is the ionization cross section used for training, $\sigma_1(\varepsilon)$ is our initial proposed ionization cross section, $\sigma_2(\varepsilon)$ is a randomly chosen LXCat ionization cross section, and ε_2 is that cross section's corresponding threshold energy, and we also introduce an energy-dependent mixing ratio that varies from 0.2 to 0.0 as the energy varies from the ionization threshold to 10^3 eV,

$$r(\varepsilon) = 0.2\frac{\ln\left(\frac{\varepsilon}{10^3\ \text{eV}}\right)}{\ln\left(\frac{9.69\ \text{eV}}{10^3\ \text{eV}}\right)}. \tag{11}$$

The resulting constrained confidence band of training examples is plotted in Fig. 13, alongside the refined fit provided by the neural network, as well as the original proposed ionization cross section. As was expected, the refined ionization cross section predicted by the neural network is smaller in magnitude, peaking at 5.5×10^{-20} m^2 compared to 15×10^{-20} m^2 for what we proposed initially. Nonetheless, such a large drop in magnitude (~2.7 times) is a little concerning, given the reputation of Bull *et al.*[80] group. However, THFA is a very difficult molecule to work with experimentally, so such a mismatch may indeed be possible in this case.

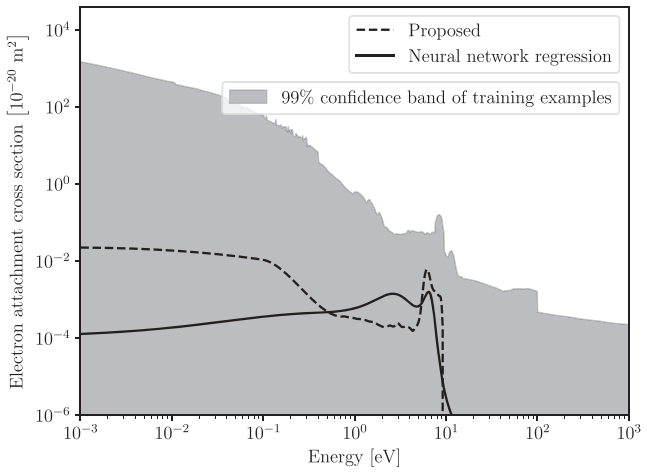

FIG. 12. Neural network regression results for the THFA dissociative electron attachment cross section, alongside the earlier proposed ICS for comparison. See also the legend in the figure.

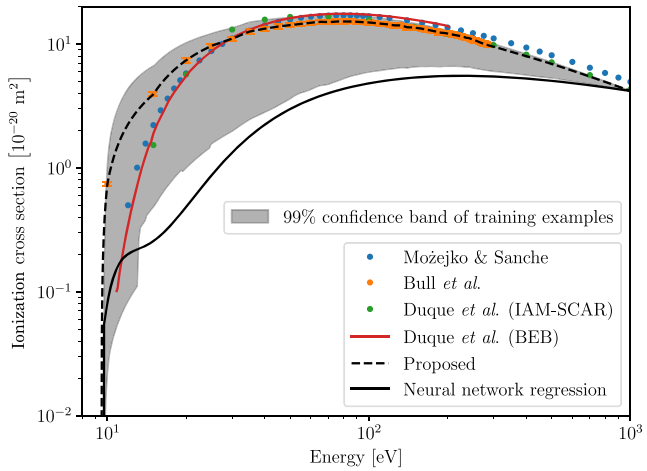

FIG. 13. Neural network regression results for the THFA electron impact ionization cross section, alongside the earlier proposed ICS and the previous experimental and theoretical results[21,79,80] from which it was derived. See also the legend in the figure.

Published under license by AIP Publishing

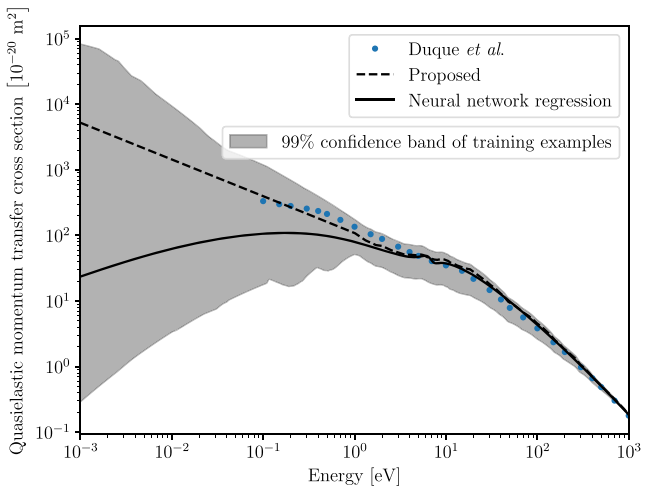

FIG. 14. Neural network regression results for the THFA quasielastic MTCS, alongside the earlier proposed MTCS for comparison. See also the legend in the figure.

D. Refined quasielastic momentum transfer cross section

As with the ionization cross section, we expect our proposed quasielastic MTCS to be most accurate at higher energies. As such, we proceed similar to our approach with ionization and sample each quasielastic MTCS for training using the following formula:

$$\sigma(\varepsilon) = \sigma_1^{1-r(\varepsilon)}(\varepsilon)\sigma_2^{r(\varepsilon)}(\varepsilon), \tag{12}$$

where $\sigma(\varepsilon)$ is the MTCS cross section used for training, $\sigma_1(\varepsilon)$ is our initial proposed quasielastic MTCS, and $\sigma_2(\varepsilon)$ is a randomly chosen LXCat elastic cross section, and we define here the energy-dependent mixing ratio that varies from 1.0 to 0.15 to 0.0 as the energy varies from 10^{-3} eV to 1 eV to 10^3 eV,

$$r(\varepsilon) = 0.15\begin{cases} 1 - \dfrac{17}{3}\dfrac{\ln\left(\frac{\varepsilon}{1\text{ eV}}\right)}{\ln\left(\frac{10^3\text{ eV}}{1\text{ eV}}\right)}, & 10^{-3}\text{ eV} \le \varepsilon \le 1\text{ eV}, \\ 1 - \dfrac{\ln\left(\frac{\varepsilon}{1\text{ eV}}\right)}{\ln\left(\frac{10^3\text{ eV}}{1\text{ eV}}\right)}, & 1\text{ eV} \le \varepsilon \le 10^3\text{ eV}. \end{cases} \tag{13}$$

The resulting constrained confidence band of training examples is plotted in Fig. 14, alongside the refined fit provided by the neural network, as well as the original proposed quasielastic MTCS. The refined quasielastic MTCS provided by the neural network is essentially identical to the proposal at energies above 1 eV. Below

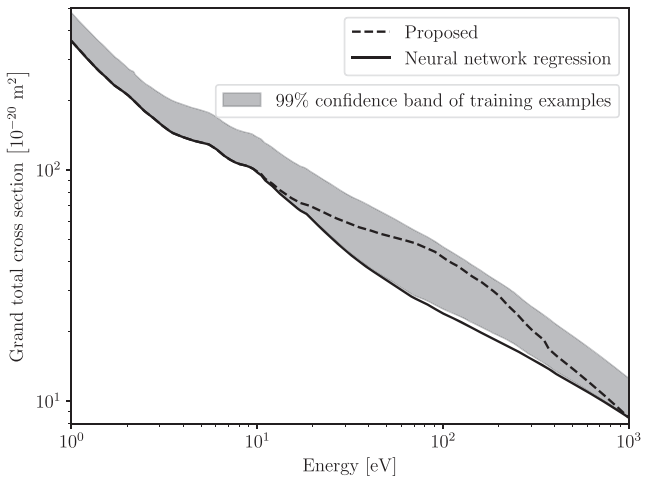

FIG. 15. Neural network regression results for the THFA grand TCS, alongside the original proposed TCS for comparison. See also the legend in the figure.

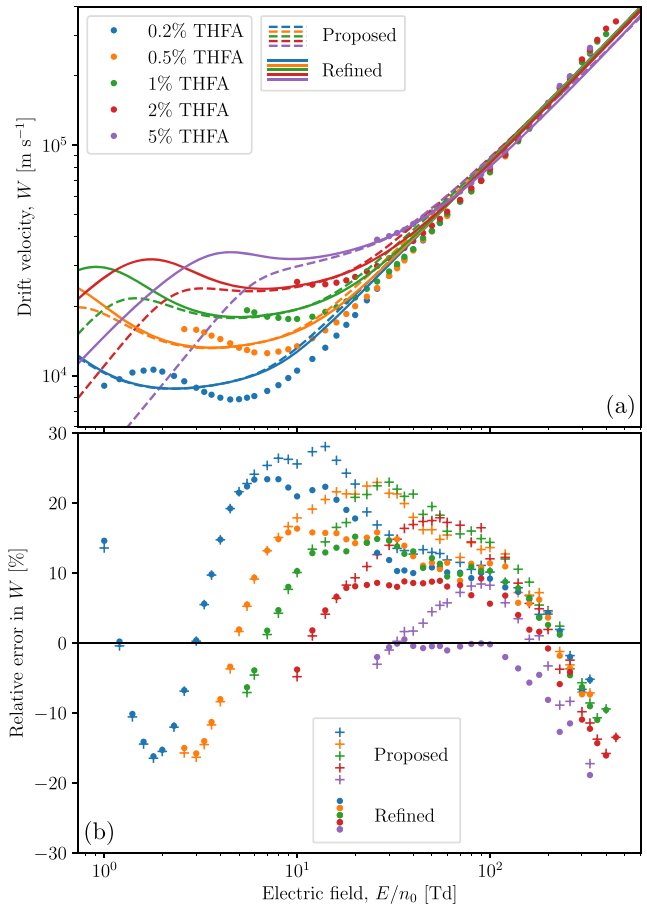

FIG. 16. (a) Simulated drift velocities from both our original proposed database and our refined database, compared to corresponding results from our admixture swarm measurements. (b) Corresponding percentage errors in the simulated values relative to the swarm measurements. See also legends in figures.

Published under license by AIP Publishing

1 eV, however, the neural network predicts quasielastic MTCS that is significantly smaller than the proposal, steadily decreasing in relative magnitude as energy is decreased. The greatest difference occurs at 10^{-3} eV, where the refined quasielastic MTCS is roughly two orders of magnitude smaller than its counterpart from our initial proposed set.

E. Refined grand total cross section

Although it is not considered explicitly, the grand TCS of each cross section set used for training is naturally affected by the aforementioned constraints placed on the neutral dissociation, attachment, and ionization cross sections. The resulting constrained confidence band of training examples is plotted in Fig. 15, alongside the refined fit provided by the neural network, as well as the original proposed grand TCS. The neural network predictions result in a grand TCS that is smaller than the initial proposal for energies above 10 eV or so while coinciding below this energy. The greatest difference arises at 90 eV with a reduction in magnitude of 43%, most of which being due to the reduction in the ionization cross section (see Fig. 13).

VI. TRANSPORT COEFFICIENTS OF THE REFINED ELECTRON-THFA CROSS SECTION SET

A. Refined admixture transport coefficients

Using our refined set of electron-THFA cross sections, we plot revised simulated transport coefficients in Figs. 16–18 for comparison to both our admixture swarm measurements and to the transport coefficients calculated previously for our initial proposed cross section set. Respectively, the drift velocities, effective Townsend first ionization coefficients, and longitudinal diffusion coefficients are each plotted in Figs. 16(a)–18(a), with corresponding percentage error differences plotted in Figs. 16(b)–18(b). Figure 16 shows that the refined set of electron-THFA cross sections has, in general, brought the simulated drift velocities closer to the results from the

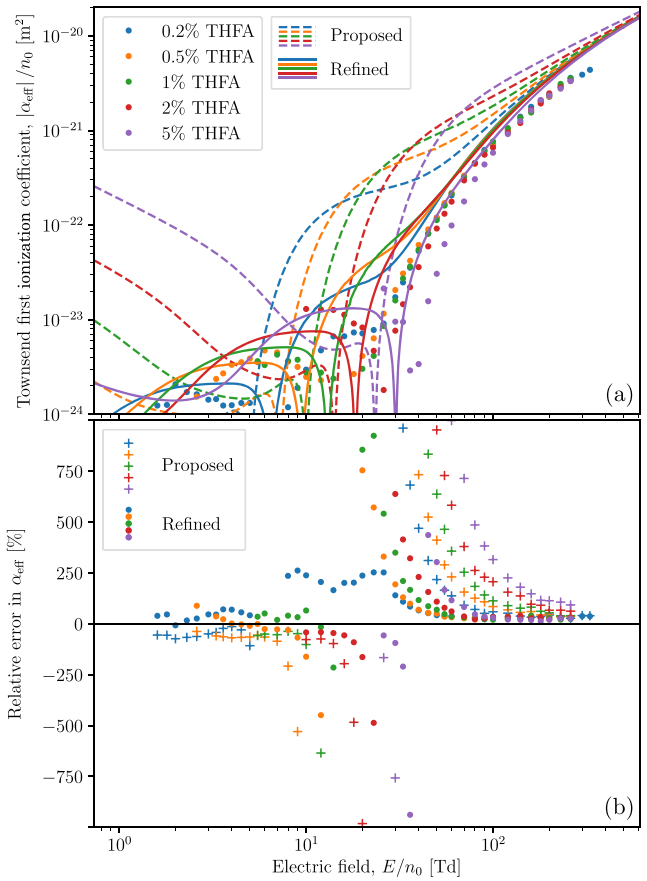

FIG. 17. (a) Simulated effective Townsend first ionization coefficients from both our original proposed database and our refined database, compared to corresponding results from our admixture swarm measurements. (b) Corresponding percentage errors in the simulated values relative to the swarm measurements. See also legends in figures.

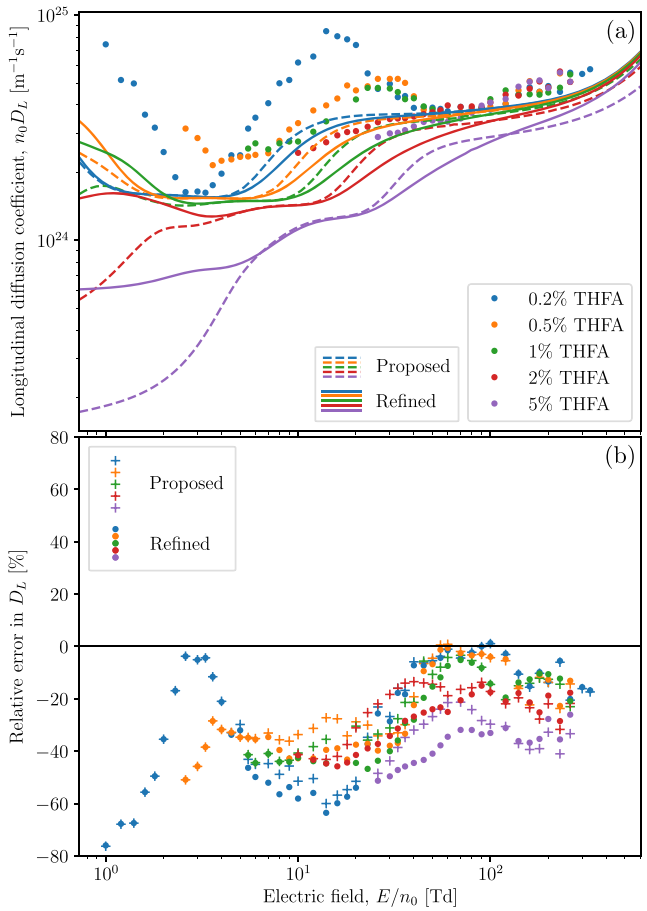

FIG. 18. (a) Simulated longitudinal diffusion coefficients from both our original proposed database and our refined database, compared to corresponding results from our admixture swarm measurements. (b) Corresponding percentage errors in the simulated values relative to the swarm measurements. See also legends in figures.

Published under license by AIP Publishing

experimental measurements. There are some instances where the mismatch has increased, but these are infrequent. The large discrepancies between simulation and experiment remain at low fields, with the refinement having very little effect on the drift velocities in this regime. Figure 17 shows a substantial improvement in the effective Townsend first ionization coefficients after the cross section refinement. Overall, both the relative error and the shape of the simulated effective Townsend first ionization coefficients have improved, with the most benefit seen in the electropositive regime. Figure 18 shows a slight worsening in the accuracy of the simulated longitudinal diffusion coefficients after the neural network refinement, contrary to the other transport coefficients. It should be noted, however, that the shape of the plotted longitudinal diffusion coefficients has appeared to improve slightly with the refined cross section dataset.

B. Transport coefficients in pure THFA

Figure 19 shows the results of using our refined cross section set to simulate electron swarm transport coefficients in pure gaseous THFA at 300 K, across a range of reduced electric fields from 0.001 Td up to 10 000 Td. We employ our multi-term Boltzmann solver here also but find the two-term approximation to be fairly sufficient for all but diffusion at the highest E/n_0 considered, which can be in error by up to 59% in the case of the bulk longitudinal diffusion coefficient. Figure 19(a) shows the mean energy of the electron swarm, alongside that for the background THFA vapor for comparison. In the low-field regime, the mean electron energy is ~26 meV, which is substantially lower than the thermal background of ~39 meV due primarily to attachment cooling. As E/n_0 increases, heating due to the field increases the mean energy of the swarm to eventually reach thermal equilibrium with the background THFA at ~0.175 Td. Beyond this E/n_0, the mean energy continues increasing monotonically, with its ascent occasionally slowing due to the onset of the excitation channels (around 0.5 Td) and the ionization channel (around 200 Td). Figure 19(b) shows rate coefficients for quasielastic momentum transfer, summed excitation, attachment, and ionization. The quasielastic momentum transfer rate coefficient remains fairly constant up until 30 Td, after which it increases slightly, likely due to the maximum in the magnitude of the quasielastic MTCS

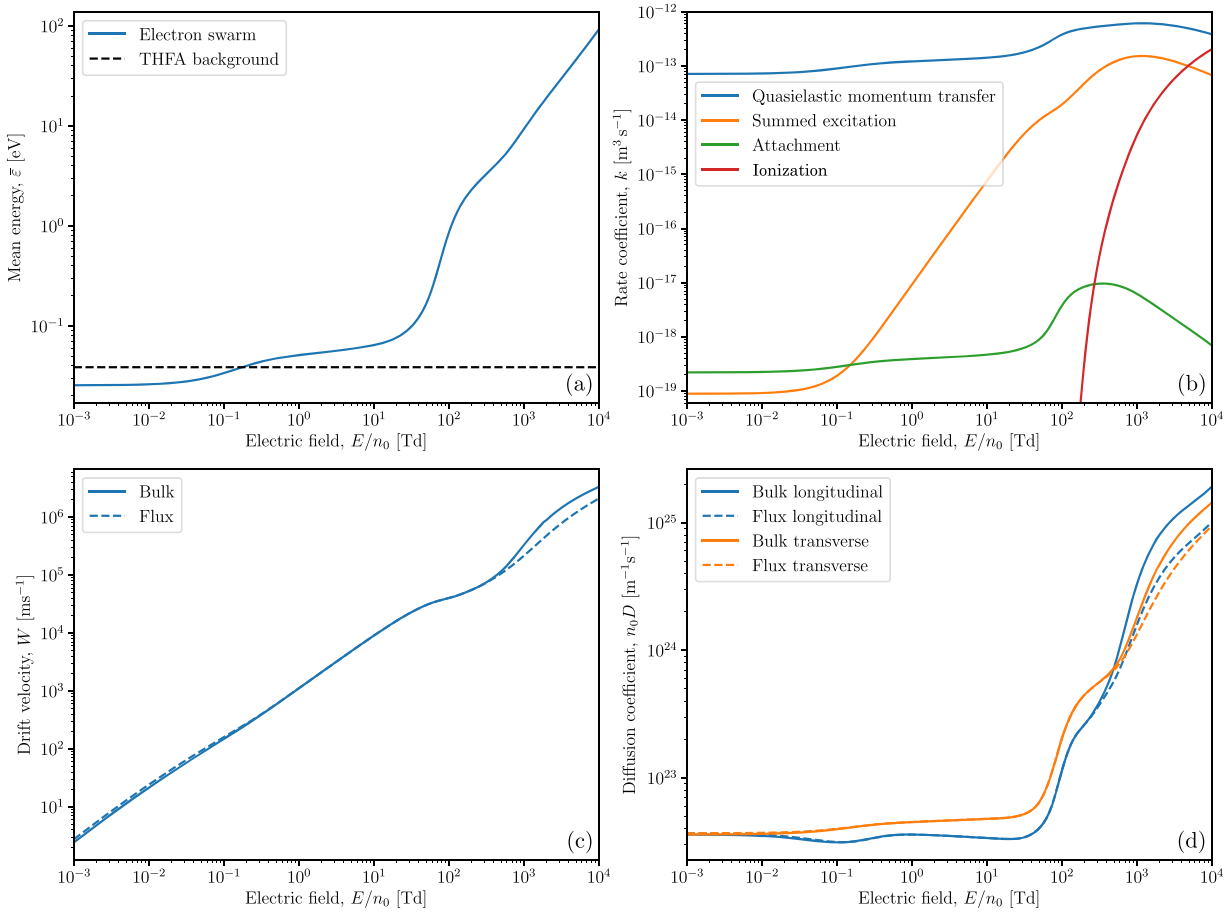

FIG. 19. Calculated mean electron energy (a), rate coefficients (b), drift velocities (c), and diffusion coefficients (d) for electrons in pure THFA vapor at 300 K over a range of reduced electric fields. See also the legends for further details.

Published under license by AIP Publishing

at ~0.18 eV. The summed excitation rate coefficient starts off constant at very low fields but begins to increase, rather early, from 5×10^{-2} Td due to the additional opening of the vibrational excitation channels. This increase continues monotonically until reaching a maximum at ~1200 Td, after which the summed excitation rate decreases slightly at very high fields. The attachment rate coefficient also starts off as being constant, before increasing monotonically to a peak at ~350 Td, likely due to the associated peaks in the attachment cross section magnitude at ~2.6 and ~6.4 eV. As there is no appreciable attachment cross section beyond ~12 eV, there is a corresponding drop in the attachment rate coefficient from this point onward. The ionization rate coefficient is zero at low fields before increasing monotonically and becoming appreciable from around 200 Td, onward. Figure 19(c) shows the bulk and flux drift velocities of the swarm, both of which are seen to increase monotonically with increasing E/n_0. At low fields, the flux drift velocity slightly exceeds the bulk, indicating that electrons are being preferentially attached at the front of the swarm and so shifting the center of mass toward the rear. At intermediate fields, between roughly 1 and 300 Td, nonconservative effects are sufficiently small such that the bulk and flux drift velocities coincide. Above 300 Td, the bulk drift velocity now exceeds the flux due to ionization preferentially creating electrons at the front of the swarm. Figure 19(d) shows the bulk and flux diffusion coefficients of the swarm in both the longitudinal and transverse directions relative to the field. As with the drift velocities, for intermediate E/n_0 between roughly 1 and 300 Td, nonconservative effects are minimal and the bulk and flux diffusion coefficients coincide. The transverse diffusion coefficient differs the least between its flux and bulk counterparts. At low fields, below 1 Td, there is only a very slight decrease in the bulk transverse diffusion compared to its flux counterpart, which we attribute to the slight preferential attachment of electrons toward the sides of the swarm. At high fields, above 300 Td, there is a substantial increase in bulk transverse diffusion over the flux, which we naturally attribute to the preferential ionization production of electrons toward the swarm sides. The bulk longitudinal coefficient follows a similar trend, for these same reasons of preferential attachment and ionization in the longitudinal direction.

VII. CONCLUSION

We have formed a complete and self-consistent set of electron-THFA cross sections by constructing an initially proposed set from the literature and then refining its least-certain aspects by measuring and analyzing electron swarm transport coefficients in admixtures of THFA in argon. Notably, this swarm analysis and cross section refinement were performed automatically and objectively using a neural network model [Eq. (1)] trained on cross sections from the LXCat project.[41–43] Our neural network determined plausible cross sections for attachment and neutral dissociation in their entirety from the measured swarm data as well as cross sections for ionization and quasielastic momentum transfer subject to constraints given by known experimental error bars. We subsequently used our Boltzmann equation solver to calculate transport coefficients for this refined cross section set and found an improved consistency with our experimental admixture measurements. We also calculated transport coefficients for electrons in pure THFA, revealing the interesting phenomenon of attachment cooling of the electron swarm below the thermal background.

Given the similar methodology and swarm measurements between the present investigation and our previous successful refinement of an electron-THF cross section set,[17] we believe our refined set of electron-THFA cross sections should be of comparable quality, if not a little better, to one hand-fitted by an expert. As there is evidently still some room for improvement, it is fortunate that this machine learning approach makes it straightforward to revisit THFA as new swarm data, cross section constraints, or LXCat training data become available.

A known limitation[17,39] of the present machine learning approach to swarm analysis is that it provides a unique solution to a problem for which multiple plausible solutions are likely to exist. In the future, we intend to address this deficiency by quantifying the uncertainty in the predicted cross sections using a suitable alternative machine learning model.[100–105] Finally, we also plan to apply our machine learning approach to determine complete and self-consistent cross section sets for other molecules of biological interest, including those for water.[6]

ACKNOWLEDGMENTS

Thanks are due to A. Bustos and G. Bustos for their technical assistance. The authors gratefully acknowledge the financial support of the Australian Research Council through the Discovery Projects Scheme (Grant No. DP180101655). J.d.U. thanks PAPIIT-UNAM (Project No. IN118520) for support. G.G. acknowledges support from the Spanish Ministerio de Ciencia, Innovación y Universidades-MICIU (Project Nos. FIS2016-80440 and PID2019-104727RB-C21) and CSIC (Project No. LINKA 20085).

APPENDIX: PULSED-TOWNSEND ELECTRON SWARM MEASUREMENT RESULTS FOR VARIOUS ADMIXTURES OF THFA IN ARGON

TABLE I. Measured pulsed-Townsend electron swarm transport coefficients for a 0.2% admixture of THFA in argon. Estimated experimental uncertainties are ±2% for drift velocities, W; ±6% for effective Townsend first ionization coefficients, α_{eff}/n_0; and ±12% for longitudinal diffusion coefficients, $n_0 D_L$.

E/n_0 (Td)	W $(10^4\ \text{m s}^{-1})$	α_{eff}/n_0 $(10^{-24}\ \text{m}^2)$	$n_0 D_L$ $(10^{24}\ \text{m}^{-1}\ \text{s}^{-1})$
1.0	0.903		7.43
1.2	0.964		5.16
1.4	1.03		4.98
1.6	1.05	−1.24	3.62
1.8	1.06	−1.26	3.17
2.0	1.04	−2.08	2.47
2.3	0.996	−1.72	1.91
2.6	0.944	−1.63	1.64
3.0	0.885	−1.43	1.65
3.3	0.849	−1.45	1.63
3.6	0.825	−1.24	1.76
4.0	0.801	−1.25	1.98

Published under license by AIP Publishing

TABLE I. *(Continued.)*

E/n_0 (Td)	W $(10^4\ \mathrm{m\,s^{-1}})$	$\alpha_{\mathrm{eff}}/n_0$ $(10^{-24}\ \mathrm{m^2})$	$n_0 D_L$ $(10^{24}\ \mathrm{m^{-1}\,s^{-1}})$
4.5	0.787	−1.32	2.39
5.0	0.789	−1.32	2.39
5.5	0.801		3.14
6.0	0.814		3.51
7.0	0.857		4.07
8.0	0.908	1.19	4.99
9.0	0.975	1.91	5.16
10	1.05	2.97	6.17
12	1.18	4.75	6.56
14	1.32	6.67	8.50
16	1.49	6.69	8.07
18	1.66	7.34	7.82
20	1.83	7.17	7.38
23	2.12	7.80	5.52
26	2.38	9.12	4.71
30	2.71	17.3	4.96
33	2.98	24.8	4.33
36	3.21	35.5	4.38
40	3.52	53.2	3.88
45	3.86	82.2	3.91
50	4.23	120	3.89
55	4.59	163	3.84
60	4.98	206	3.75
70	5.69	325	3.92
80	6.43	454	3.87
90	7.07	623	3.82
100	7.80	707	3.81
120	9.23	996	4.04
140	10.6	1400	4.45
160	12.0	1780	4.79
180	13.6	2070	4.58
200	14.8	2270	4.85
230	17.1	2900	4.57
260	19.7	3600	5.56
300	23.4	3890	5.49
330	25.0	4380	5.76

TABLE II. *(Continued.)*

E/n_0 (Td)	W $(10^4\ \mathrm{m\,s^{-1}})$	$\alpha_{\mathrm{eff}}/n_0$ $(10^{-24}\ \mathrm{m^2})$	$n_0 D_L$ $(10^{24}\ \mathrm{m^{-1}\,s^{-1}})$
5.0	1.32	−3.89	2.35
5.5	1.29	−3.55	2.36
6.0	1.26	−4.73	2.40
7.0	1.25	−4.52	2.44
8.0	1.27	−3.62	2.77
9.0	1.30	−3.17	3.11
10	1.34	−2.49	3.32
12	1.45	−2.29	3.78
14	1.57		3.98
16	1.70		4.27
18	1.85	2.67	4.88
20	2.00	4.14	4.64
23	2.20	6.36	4.84
26	2.40	11.6	5.22
30	2.71	20.6	5.22
33	2.92	30.8	5.22
36	3.16	42.0	5.01
40	3.49	61.8	4.37
45	3.89	90.2	3.80
50	4.23	120	3.74
55	4.62	171	3.57
60	4.93	219	3.58
70	5.75	334	3.72
80	6.30	445	3.81
90	7.00	560	3.84
100	7.62	727	3.93
120	8.94	1020	4.05
140	10.7	1360	4.64
160	12.0	1590	5.10
180	13.2	2080	4.57
200	14.8	2300	4.75
230	17.6	3010	5.52
260	19.9	3500	5.06
300	23.4		
330	25.4		

TABLE II. Measured pulsed-Townsend electron swarm transport coefficients for a 0.5% admixture of THFA in argon. The estimated experimental uncertainties are ±2% for drift velocities, W; ± 6% for effective Townsend first ionization coefficients, $\alpha_{\mathrm{eff}}/n_0$; and ±12% for longitudinal diffusion coefficients, $n_0 D_L$.

E/n_0 (Td)	W $(10^4\ \mathrm{m\,s^{-1}})$	$\alpha_{\mathrm{eff}}/n_0$ $(10^{-24}\ \mathrm{m^2})$	$n_0 D_L$ $(10^{24}\ \mathrm{m^{-1}\,s^{-1}})$
2.6	1.59	−1.54	3.14
3.0	1.58		2.85
3.3	1.54	−2.37	2.51
3.6	1.49	−2.71	2.16
4.0	1.44	−3.34	2.26
4.5	1.38	−3.56	2.29

TABLE III. Measured pulsed-Townsend electron swarm transport coefficients for a 1% admixture of THFA in argon. The estimated experimental uncertainties are ±2% for drift velocities, W; ±6% for effective Townsend first ionization coefficients, $\alpha_{\mathrm{eff}}/n_0$; and ±12% for longitudinal diffusion coefficients, $n_0 D_L$.

E/n_0 (Td)	W $(10^4\ \mathrm{m\,s^{-1}})$	$\alpha_{\mathrm{eff}}/n_0$ $(10^{-24}\ \mathrm{m^2})$	$n_0 D_L$ $(10^{24}\ \mathrm{m^{-1}\,s^{-1}})$
5.5	1.92	−3.65	2.56
6.0	1.88	−3.32	2.70
7.0	1.80	−4.28	2.54
8.0	1.78	−3.66	2.70
9.0	1.76	−3.78	2.75
10	1.76	−2.78	2.75

Published under license by AIP Publishing

TABLE III. *(Continued.)*

E/n_0 (Td)	W $(10^4\ \mathrm{m\,s^{-1}})$	$\alpha_{\mathrm{eff}}/n_0$ $(10^{-24}\ \mathrm{m^2})$	$n_0 D_L$ $(10^{24}\ \mathrm{m^{-1}\,s^{-1}})$
12	1.80	−2.76	3.04
14	1.89	−2.39	3.38
16	1.98		
18	2.10		
20	2.18	3.03	4.23
23	2.38	4.15	4.76
26	2.56	8.58	4.76
30	2.83	16.0	4.73
33	3.05	27.3	4.56
36	3.28	36.5	4.24
40	3.54	55.0	4.28
45	3.96	80.9	3.94
50	4.25	113	3.83
55	4.62	161	3.74
60	5.04	215	3.62
70	5.70	320	3.63
80	6.31	454	3.75
90	7.00	603	3.90
100	7.65	767	4.24
120	9.05	1060	4.64
140	10.4	1360	4.43
160	11.8	1550	4.46
180	13.4	2010	4.44
200	14.8	2390	4.54
230	16.9	3110	4.77
260	19.9	3560	5.46
300	22.9		
330	25.6		
360	28.2		
400	30.4		

TABLE IV. Measured pulsed-Townsend electron swarm transport coefficients for a 2% admixture of THFA in argon. The estimated experimental uncertainties are ±2% for drift velocities, W; ±6% for effective Townsend first ionization coefficients, $\alpha_{\mathrm{eff}}/n_0$; and ±12% for longitudinal diffusion coefficients, $n_0 D_L$.

E/n_0 (Td)	W $(10^4\ \mathrm{m\,s^{-1}})$	$\alpha_{\mathrm{eff}}/n_0$ $(10^{-24}\ \mathrm{m^2})$	$n_0 D_L$ $(10^{24}\ \mathrm{m^{-1}\,s^{-1}})$
10	2.55	−13.0	2.45
12	2.48	−12.8	2.57
14	2.49	−12.7	2.73
16	2.53	−11.3	2.93
18	2.59	−9.13	3.03
20	2.68	−8.29	3.06
23	2.83	−4.70	3.20
26	2.99	−1.81	3.35
30	3.23	7.66	3.46
33	3.42	14.6	3.48
36	3.58	22.1	3.49
40	3.84	36.0	3.55

TABLE IV. *(Continued.)*

E/n_0 (Td)	W $(10^4\ \mathrm{m\,s^{-1}})$	$\alpha_{\mathrm{eff}}/n_0$ $(10^{-24}\ \mathrm{m^2})$	$n_0 D_L$ $(10^{24}\ \mathrm{m^{-1}\,s^{-1}})$
45	4.16	59.6	3.64
50	4.48	92.1	3.71
55	4.79	132	3.79
60	5.15	177	3.98
70	5.79	297	3.92
80	6.52	449	3.94
90	7.01	556	3.89
100	7.90	661	4.10
120	9.08	950	4.44
140	10.6	1200	4.40
160	12.1	1660	4.72
180	13.4	1930	5.08
200	15.0	2470	4.79
230	17.8	2860	5.63
260	19.4	3340	5.06
300	23.6		
330	26.0		
360	28.7		
400	32.1		
450	34.5		

TABLE V. Measured pulsed-Townsend electron swarm transport coefficients for a 5% admixture of THFA in argon. The estimated experimental uncertainties are ±2% for drift velocities, W; ±6% for effective Townsend first ionization coefficients, $\alpha_{\mathrm{eff}}/n_0$; and ±12% for longitudinal diffusion coefficients, $n_0 D_L$.

E/n_0 (Td)	W $(10^4\ \mathrm{m\,s^{-1}})$	$\alpha_{\mathrm{eff}}/n_0$ $(10^{-24}\ \mathrm{m^2})$	$n_0 D_L$ $(10^{24}\ \mathrm{m^{-1}\,s^{-1}})$
26	3.89	−21.4	2.88
30	4.03	−9.54	2.99
33	4.16	−9.47	3.01
36	4.29	−2.91	3.09
40	4.55	3.40	3.21
45	4.84	15.7	3.36
50	5.11	30.6	3.41
55	5.40	63.0	3.40
60	5.73	99.1	3.37
70	6.30	178	3.48
80	6.88	306	3.69
90	7.48	438	3.97
100	8.10	582	4.10
120	9.49	918	4.25
140	10.9	1260	4.82
160	12.4	1630	5.07
180	13.5	2100	5.14
200	15.3	2350	4.75
230	18.1	2770	5.57
260	19.8	3330	5.07
330	26.5		

Published under license by AIP Publishing

DATA AVAILABILITY

The data that support the findings of this study are available within the article.

REFERENCES

[1] G. G. Gómez-Tejedor and M. C. Fuss, *Radiation Damage in Biomolecular Systems* (Springer Science & Business Media, 2012).
[2] B. Boudaïffa, P. Cloutier, D. Hunting, M. A. Huels, and L. Sanche, Science **287**, 1658–1660 (2000).
[3] M. G. Kong, G. Kroesen, G. Morfill, T. Nosenko, T. Shimizu, J. van Dijk, and J. L. Zimmermann, New J. Phys. **11**, 115012 (2009).
[4] P. J. Bruggeman, M. J. Kushner, B. R. Locke, J. G. E. Gardeniers, W. G. Graham, D. B. Graves, R. C. H. M. Hofman-Caris, D. Maric, J. P. Reid, E. Ceriani, D. Fernandez Rivas, J. E. Foster, S. C. Garrick, Y. Gorbanev, S. Hamaguchi, F. Iza, H. Jablonowski, E. Klimova, J. Kolb, F. Krcma, P. Lukes, Z. Machala, I. Marinov, D. Mariotti, S. Mededovic Thagard, D. Minakata, E. C. Neyts, J. Pawlat, Z. L. Petrovic, R. Pflieger, S. Reuter, D. C. Schram, S. Schröter, M. Shiraiwa, B. Tarabová, P. A. Tsai, J. R. R. Verlet, T. von Woedtke, K. R. Wilson, K. Yasui, and G. Zvereva, Plasma Sources Sci. Technol. **25**, 053002 (2016).
[5] I. Adamovich, S. D. Baalrud, A. Bogaerts, P. J. Bruggeman, M. Cappelli, V. Colombo, U. Czarnetzki, U. Ebert, J. G. Eden, P. Favia, D. B. Graves, S. Hamaguchi, G. Hieftje, M. Hori, I. D. Kaganovich, U. Kortshagen, M. J. Kushner, N. J. Mason, S. Mazouffre, S. M. Thagard, H.-R. Metelmann, A. Mizuno, E. Moreau, A. B. Murphy, B. A. Niemira, G. S. Oehrlein, Z. L. Petrovic, L. C. Pitchford, Y.-K. Pu, S. Rauf, O. Sakai, S. Samukawa, S. Starikovskaia, J. Tennyson, K. Terashima, M. M. Turner, M. C. M. van de Sanden, and A. Vardelle, J. Phys. D: Appl. Phys. **50**, 323001 (2017).
[6] R. D. White, M. J. Brunger, N. A. Garland, R. E. Robson, K. F. Ness, G. Garcia, J. de Urquijo, S. Dujko, and Z. L. Petrović, Eur. Phys. J. D **68**, 125 (2014).
[7] H. Nikjoo, S. Uehara, D. Emfietzoglou, and F. A. Cucinotta, Radiat. Meas. **41**, 1052–1074 (2006).
[8] Z. Francis, S. Incerti, R. Capra, B. Mascialino, G. Montarou, V. Stepan, and C. Villagrasa, Appl. Radiat. Isot. **69**, 220–226 (2011).
[9] M. J. Brunger, Int. Rev. Phys. Chem. **36**, 333–376 (2017).
[10] N. A. Garland, M. J. Brunger, G. Garcia, J. de Urquijo, and R. D. White, Phys. Rev. A **88**, 062712 (2013).
[11] M. C. Fuss, A. G. Sanz, F. Blanco, P. Limão-Vieira, M. J. Brunger, and G. García, Eur. Phys. J. D **68**, 161 (2014).
[12] M. U. Bug, W. Yong Baek, H. Rabus, C. Villagrasa, S. Meylan, and A. B. Rosenfeld, Radiat. Phys. Chem. **130**, 459–479 (2017).
[13] M. Swadia, Y. Thakar, M. Vinodkumar, and C. Limbachiya, Eur. Phys. J. D **71**, 85 (2017).
[14] M. Swadia, R. Bhavsar, Y. Thakar, M. Vinodkumar, and C. Limbachiya, Mol. Phys. **115**, 2521–2527 (2017).
[15] M. J. E. Casey, J. de Urquijo, L. N. Serkovic Loli, D. G. Cocks, G. J. Boyle, D. B. Jones, M. J. Brunger, and R. D. White, J. Chem. Phys. **147**, 195103 (2017).
[16] J. de Urquijo, M. J. E. Casey, L. N. Serkovic-Loli, D. G. Cocks, G. J. Boyle, D. B. Jones, M. J. Brunger, and R. D. White, J. Chem. Phys. **151**, 054309 (2019).
[17] P. W. Stokes, M. J. E. Casey, D. G. Cocks, J. de Urquijo, G. García, M. J. Brunger, and R. D. White, Plasma Sources Sci. Technol. **29**, 105008 (2020).
[18] R. D. White and R. E. Robson, Phys. Rev. Lett. **102**, 230602 (2009).
[19] R. D. White, W. Tattersall, G. Boyle, R. E. Robson, S. Dujko, Z. L. Petrovic, A. Bankovic, M. J. Brunger, J. P. Sullivan, S. J. Buckman, and G. Garcia, Appl. Radiat. Isot. **83**, 77–85 (2014).
[20] P. Limão-Vieira, D. Duflot, M.-J. Hubin-Franskin, J. Delwiche, S. V. Hoffmann, L. Chiari, D. B. Jones, M. J. Brunger, and M. C. A. Lopes, J. Phys. Chem. A **118**, 6425–6434 (2014).
[21] H. V. Duque, L. Chiari, D. B. Jones, P. A. Thorn, Z. Pettifer, G. B. da Silva, P. Limão-Vieira, D. Duflot, M.-J. Hubin-Franskin, J. Delwiche, F. Blanco, G. García, M. C. A. Lopes, K. Ratnavelu, R. D. White, and M. J. Brunger, Chem. Phys. Lett. **608**, 161–166 (2014).
[22] R. D. White, D. Cocks, G. Boyle, M. Casey, N. Garland, D. Konovalov, B. Philippa, P. Stokes, J. de Urquijo, O. González-Magaña, R. P. McEachran, S. J. Buckman, M. J. Brunger, G. Garcia, S. Dujko, and Z. L. Petrovic, Plasma Sources Sci. Technol. **27**, 053001 (2018).
[23] H. F. Mayer, Ann. Phys. **369**, 451–480 (1921).
[24] C. Ramsauer, Ann. Phys. **369**, 513–540 (1921).
[25] J. S. Townsend and V. A. Bailey, London, Edinburgh, Dublin Philos. Mag. J. Sci. **43**, 593–600 (1922).
[26] L. S. Frost and A. V. Phelps, Phys. Rev. **127**, 1621–1633 (1962).
[27] A. G. Engelhardt and A. V. Phelps, Phys. Rev. **131**, 2115–2128 (1963).
[28] A. G. Engelhardt, A. V. Phelps, and C. G. Risk, Phys. Rev. **135**, A1566–A1574 (1964).
[29] R. D. Hake and A. V. Phelps, Phys. Rev. **158**, 70–84 (1967).
[30] A. V. Phelps, Rev. Mod. Phys. **40**, 399–410 (1968).
[31] C. W. Duncan and I. C. Walker, J. Chem. Soc., Faraday Trans. 2 **68**, 1514 (1972).
[32] T. F. O'Malley and R. W. Crompton, J. Phys. B: At. Mol. Phys. **13**, 3451–3464 (1980).
[33] T. Taniguchi, M. Suzuki, K. Kawamura, F. Noto, and H. Tagashira, J. Phys. D: Appl. Phys. **20**, 1085–1087 (1987).
[34] M. Suzuki, T. Taniguchi, and H. Tagashira, J. Phys. D: Appl. Phys. **22**, 1848–1855 (1989).
[35] M. Suzuki, T. Taniguchi, and H. Tagashira, J. Phys. D: Appl. Phys. **23**, 842–850 (1990).
[36] W. L. Morgan, Phys. Rev. A **44**, 1677–1681 (1991).
[37] W. L. Morgan, J. Phys. D: Appl. Phys. **26**, 209–214 (1993).
[38] M. Brennan and K. Ness, Aust. J. Phys. **46**, 249 (1993).
[39] P. W. Stokes, D. G. Cocks, M. J. Brunger, and R. D. White, Plasma Sources Sci. Technol. **29**, 055009 (2020).
[40] W. L. Morgan, IEEE Trans. Plasma Sci. **19**, 250–255 (1991).
[41] S. Pancheshnyi, S. Biagi, M. C. Bordage, G. J. M. Hagelaar, W. L. Morgan, A. V. Phelps, and L. C. Pitchford, Chem. Phys. **398**, 148–153 (2012).
[42] L. C. Pitchford, L. L. Alves, K. Bartschat, S. F. Biagi, M.-C. Bordage, I. Bray, C. E. Brion, M. J. Brunger, L. Campbell, A. Chachereau, B. Chaudhury, L. G. Christophorou, E. Carbone, N. A. Dyatko, C. M. Franck, D. V. Fursa, R. K. Gangwar, V. Guerra, P. Haefliger, G. J. M. Hagelaar, A. Hoesl, Y. Itikawa, I. V. Kochetov, R. P. McEachran, W. L. Morgan, A. P. Napartovich, V. Puech, M. Rabie, L. Sharma, R. Srivastava, A. D. Stauffer, J. Tennyson, J. de Urquijo, J. van Dijk, L. A. Viehland, M. C. Zammit, O. Zatsarinny, and S. Pancheshnyi, Plasma Processes Polym. **14**, 1600098 (2017).
[43] See www.lxcat.net for LXCat.
[44] J. Nam, H. Yong, J. Hwang, and J. Choi, Phys. Lett. A **387**, 127005 (2021).
[45] R. P. McEachran, B. P. Marinković, G. García, R. D. White, P. W. Stokes, D. B. Jones, and M. J. Brunger, J. Phys. Chem. Ref. Data **49**, 013102 (2020).
[46] F. Blanco, G. García, R. P. McEachran, P. W. Stokes, R. D. White, and M. J. Brunger, J. Phys. Chem. Ref. Data **48**, 033103 (2019).
[47] R. P. McEachran, F. Blanco, G. García, P. W. Stokes, R. D. White, and M. J. Brunger, J. Phys. Chem. Ref. Data **47**, 043104 (2018).
[48] M. J. Brunger and S. J. Buckman, Phys. Rep. **357**, 215–458 (2002).
[49] D. Misra, arXiv:1908.08681 (2019).
[50] See www.lxcat.net/Biagi for Biagi database.
[51] See www.lxcat.net/Biagi-v7.1 for Biagi-v7.1 database.
[52] See www.lxcat.net/Bordage for Bordage database.
[53] See www.lxcat.net/BSR for BSR database.
[54] See www.lxcat.net/CCC for CCC database.
[55] See www.lxcat.net/Christophorou for Christophorou database.
[56] See www.lxcat.net/COP for COP database.
[57] See www.lxcat.net/eMol-LeHavre for eMol-LeHavre database.
[58] See www.lxcat.net/FLINDERS for FLINDERS database.
[59] See www.lxcat.net/Hayashi for Hayashi database.
[60] See www.lxcat.net/IST-Lisbon for IST-Lisbon database.
[61] See www.lxcat.net/Itikawa for Itikawa database.

Published under license by AIP Publishing

[62]See www.lxcat.net/Morgan for Morgan database.
[63]See www.lxcat.net/NGFSRDW for NGFSRDW database.
[64]See www.lxcat.net/Phelps for Phelps database.
[65]See www.lxcat.net/Puech for Puech database.
[66]See www.lxcat.net/QUANTEMOL for QUANTEMOL database.
[67]See www.lxcat.net/SIGLO for SIGLO database.
[68]See www.lxcat.net/TRINITI for TRINITI database.
[69]R. D. White, R. E. Robson, S. Dujko, P. Nicoletopoulos, and B. Li, J. Phys. D: Appl. Phys. **42**, 194001 (2009).
[70]G. J. Boyle, W. J. Tattersall, D. G. Cocks, R. P. McEachran, and R. D. White, Plasma Sources Sci. Technol. **26**, 024007 (2017).
[71]M. Innes, J. Open Source Software **3**, 602 (2018).
[72]X. Glorot and Y. Bengio, "Understanding the difficulty of training deep feedforward neural networks," in *Proceedings of the Thirteenth International Conference on Artificial Intelligence and Statistics*, edited by Y. W. Teh and M. Titterington (Proceedings of Machine Learning Research, PMLR, Chia Laguna Resort, Sardinia, Italy, 2010), Vol. 9, pp. 249–256.
[73]D. P. Kingma and J. L. Ba, "Adam: A method for stochastic optimization," in 3rd International Conference on Learning Representations, 2015; preprint arXiv:1412.6980.
[74]L. Chiari, H. V. Duque, D. B. Jones, P. A. Thorn, Z. Pettifer, G. B. da Silva, P. Limão-Vieira, D. Duflot, M.-J. Hubin-Franskin, J. Delwiche, F. Blanco, G. García, M. C. A. Lopes, K. Ratnavelu, R. D. White, and M. J. Brunger, J. Chem. Phys. **141**, 024301 (2014).
[75]H. V. Duque, L. Chiari, D. B. Jones, Z. Pettifer, G. B. da Silva, P. Limão-Vieira, F. Blanco, G. García, R. D. White, M. C. A. Lopes, and M. J. Brunger, J. Chem. Phys. **140**, 214306 (2014).
[76]M. A. Khakoo, D. Orton, L. R. Hargreaves, and N. Meyer, Phys. Rev. A **88**, 012705 (2013).
[77]M. Allan, J. Phys. B: At., Mol. Opt. Phys. **40**, 3531–3544 (2007).
[78]C. H. Reinsch, Numerische Math. **10**, 177–183 (1967).
[79]P. Možejko and L. Sanche, Radiat. Phys. Chem. **73**, 77–84 (2005).
[80]J. N. Bull, J. W. L. Lee, and C. Vallance, Phys. Chem. Chem. Phys. **16**, 10743–10752 (2014).
[81]H. Tanaka, M. J. Brunger, L. Campbell, H. Kato, M. Hoshino, and A. R. P. Rau, Rev. Mod. Phys. **88**, 025004 (2016).
[82]L. Chiari, A. Zecca, G. García, F. Blanco, and M. J. Brunger, J. Phys. B: At., Mol. Opt. Phys. **46**, 235202 (2013).
[83]M. Dampc, B. Mielewska, M. R. F. Siggel-King, G. C. King, and M. Zubek, Chem. Phys. Lett. **679**, 15–20 (2017).
[84]K. Aflatooni, A. M. Scheer, and P. D. Burrow, J. Chem. Phys. **125**, 054301 (2006).
[85]R. Janečková, O. May, A. Milosavljević, and J. Fedor, Int. J. Mass Spectrom. **365-366**, 163–168 (2014).
[86]A. Zecca, L. Chiari, A. Sarkar, and M. J. Brunger, J. Phys. B: At., Mol. Opt. Phys. **41**, 085201 (2008).
[87]V. Vizcaino, J. Roberts, J. P. Sullivan, M. J. Brunger, S. J. Buckman, C. Winstead, and V. McKoy, New J. Phys. **10**, 053002 (2008).
[88]A. R. Milosavljević, F. Blanco, D. Šević, G. García, and B. P. Marinković, Eur. Phys. J. D **40**, 107–114 (2006).
[89]P. Możejko, A. Domaracka, E. Ptasińska-Denga, and C. Szmytkowski, Chem. Phys. Lett. **429**, 378–381 (2006).
[90]A. Zecca, L. Chiari, G. García, F. Blanco, E. Trainotti, and M. J. Brunger, New J. Phys. **13**, 063019 (2011).
[91]A. Jain, J. Phys. B: At., Mol. Opt. Phys. **21**, 905–924 (1988).
[92]S. J. Buckman, M. J. Brunger, and K. Ratnavelu, Fusion Sci. Technol. **63**, 385–391 (2013).
[93]J. L. Hern ndez vila, E. Basurto, and J. de Urquijo, J. Phys. D: Appl. Phys. **35**, 2264–2269 (2002).
[94]E. Basurto, J. L. Hernández-Ávila, A. M. Juárez, and J. de Urquijo, J. Phys. D: Appl. Phys. **46**, 355207 (2013).
[95]J. r. Brambring, Z. Phys. **179**, 532–538 (1964).
[96]A. Bekstein, J. de Urquijo, J. L. Hernández-Ávila, and E. Basurto, Eur. Phys. J. D **66**, 77 (2012).
[97]J. de Urquijo-Carmona, "Determination of discharge parameters in sulphur hexafluoride and oxygen by observation of laser light initiated electron swarms," Ph.D. thesis, University of Manchester, 1980.
[98]M. Casey, P. Stokes, D. Cocks, D. Bošnjaković, I. Simonovic, M. Brunger, S. Dujko, Z. Petrovic, R. Robson, and R. White, "Foundations and interpretations of the pulsed-Townsend experiment," Plasma Sources Sci. Technol. (published online).
[99]R. D. White, R. E. Robson, B. Schmidt, and M. A. Morrison, J. Phys. D: Appl. Phys. **36**, 3125–3131 (2003).
[100]C. M. Bishop, Mixture density networks http://publications.aston.ac.uk/id/eprint/373/, 1994.
[101]K. Sohn, H. Lee, and X. Yan, "Learning structured output representation using deep conditional generative models," in *Advances in Neural Information Processing Systems*, edited by C. Cortes, N. D. Lawrence, D. D. Lee, M. Sugiyama, and R. Garnett (Curran Associates, Inc., 2015), Vol. 28, pp. 3483–3491.
[102]M. Mirza and S. Osindero, arXiv:1411.1784 (2014).
[103]L. Dinh, D. Krueger, and Y. Bengio, in 3rd International Conference on Learning Representations, ICLR 2015 - Workshop Track Proceedings, 2015; arXiv:1410.8516.
[104]L. Dinh, J. Sohl-Dickstein, and S. Bengio, arXiv:1605.08803 (2016).
[105]D. P. Kingma and P. Dhariwal, *Glow: Generative Flow with Invertible 1×1 Convolutions Advances in Neural Information Processing Systems*, edited by S. Bengio, H. Wallach, H. Larochelle, K. Grauman, N. Cesa-Bianchi, and R. Garnett (Curran Associates, Inc., 2018), Vol. 31, pp. 10215–10224.

Published under license by AIP Publishing